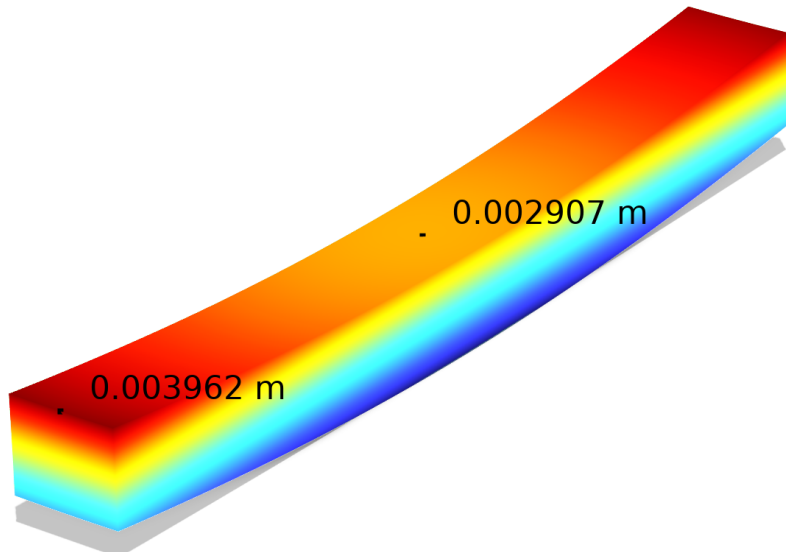


Modelling Warpage Development in SLS-Printed Parts Using a Flash Heating Approach

Anton Østergaard Thorsen

Master's thesis

June 4th, 2025



Name	Position	Student Number	Contacts
Anton Østergaard Thorsen	Master Student in Mechanical Engineering	202004932	anton-thorsen@hotmail.com
Supervisor	Position	-	Contacts
Michael Sandberg	Tenure Track Assistant Professor Aarhus University	-	ms@mpe.au.dk
Co-Supervisors	Position	-	Contacts
Michal Budzik	Associate Professor Aarhus University	-	mibu@mpe.au.dk

Anton Østergaard Thorsen

Modelling Warpage Development in SLS-Printed Parts Using a Flash Heating Approach

Master's thesis

June 2025

Aarhus University

Department of Mechanical and Production Engineering

Katrinebjergvej 89 G-F

8200 Aarhus N, Denmark

<https://www.mpe.au.dk>

This document was typeset in L^AT_EX.

ABSTRACT

This thesis investigates the applicability of using a thermo-mechanical flash heating model for predicting warpage in the selective laser sintering (SLS) process. The model, consisting of a simple beam geometry, was evaluated against experimental results obtained from a commercial SLS system. The simulation captures key thermal and mechanical behavior — including the steep temperature gradients, the temperature-dependent material properties, and the different strain components, which include the viscoplastic strains and the strains caused by the temperature-dependent density. The simulation underestimates the warpage of the experiments by 10.58%, as such, the simulation manages to capture the experimental results with a reasonable degree of accuracy. The discrepancy is likely due to the flash heating setup logic, which inherently omits the strain contribution of the layer currently being sintered and therefore undershoots the true value. Additionally, it is likely that contributing to the discrepancy of 10.58% is that some of the input data, such as heat transfer coefficients, viscoplastic properties, and densification behavior, were adopted from literature rather than derived from experimental characterization of the actual material or printer setup. Despite this, the model demonstrates the potential of estimating warpage in SLS prints for simple geometries where localized accuracy is less critical. Particularly for applications involving batch production of long, slender parts, the framework could potentially be used to assess print orientation strategies and cooling optimization. With further development, which includes optimizing the computational time, this approach may offer a computationally efficient alternative to more detailed scan-based simulations.



RESUMÉ

Dette speciale undersøger anvendeligheden af en termomekanisk flash-heating model til at forudsige deformation (warpage) i selective laser sintering (SLS) processen. Ved at anvende en simpel bjælkegeometri blev modellen evalueret mod eksperimentelle resultater fra et kommersIELT SLS system. Simuleringen formår at indfange de centrale termiske og mekaniske responsmønstre — dette inkluderer de skarpe temperaturgradienter, de temperaturafhængige materialegenskaber og de forskellige tøjningskomponenter, herunder de viskoplastiske tøjninger samt tøjninger forårsaget af den temperaturafhængige densitet. Simuleringen formår at efterligne de eksperimentelle resultater med en acceptabel præcision, men undervurderer dog den observerede deformation med 10.58%. Denne afvigelse skyldes sandsynligvis, at logikken bag flash heating modellen grundlæggende udelader bidraget fra deformationen i det lag, der aktuelt sintres, og derfor undervurderer den samlede deformation. Derudover bidrager usikkerheder i noget af inputdataen, såsom varmeoverførselskoefficienter, viskoplastiske egenskaber og densitsændringer, sandsynligvis også til afvigelsen på 10.58%, da disse data er hentet fra litteraturen og ikke er baseret på eksperimentel karakterisering af det specifikke materiale eller det specifikke printer-setup. På trods af disse begrænsninger viser modellen et potentiale for at estimere deformation i SLS-print for simple geometrier, hvor lokal nøjagtighed er mindre kritisk. I forbindelse med stor-skala produktion af lange, slanke emner kan modellen potentielt anvendes til at evaluere printorientering og optimere køleforhold. Med videreudvikling, der inkluderer optimering af beregningstid, kan denne tilgang potentielt tilbyde et beregningseffektivt alternativ til mere detaljerede scanningsbaserede simuleringer.



CONTENTS

Nomenclature

1	Introduction to Selective Laser Sintering (SLS)	1
1.1	Selective Laser Sintering	1
2	Modelling Framework	5
2.1	Materials in SLS-printing	5
2.2	Thermal Modelling	5
2.2.1	Thermal Boundary Conditions in the SLS Process	6
Heating Phase	7	
Cooling Phase	8	
2.2.2	Thermal Properties of PA12	9
2.3	Modelling of the Solid Mechanics	12
2.3.1	Viscoplasticity	13
2.3.2	Mechanical Boundary Conditions in the SLS Process	16
2.3.3	Mechanical Properties of PA12	16
3	Simulation Considerations	18
3.1	Flash Heating Simulation	18
3.1.1	Volumetric Heat Source	19
3.1.2	Laser Movement Along Build Direction	20
3.2	Activation	22
3.3	Meshing and Time-stepping	27
3.3.1	Element Discretization Type	28
3.4	Experiments	31
3.4.1	Printing of Specimens	31
3.4.2	Cooling Experiment	32
3.4.3	Measurements	32

3.4.4	Bridge Curvature Method	33
4	Results and Discussion	35
4.1	Simulation Results	35
4.1.1	Numerical Analysis	44
4.1.2	Converged Results	48
4.1.3	Experimental Results	51
4.1.4	Bridge Geometry	53
4.1.5	Parameter Study	54
5	Discussion	56
6	Conclusion	59
7	Future work	60
A	Appendix: Experimental Measurements	64

LIST OF FIGURES

Figure 1	Schematic of the SLS printer and its components. Adapted from [1].	2
Figure 2	Illustration of the SLS printer and the boundary conditions during the heating phase. Note, dimensions are not to size. Adapted from [1].	7
Figure 3	Boundary conditions during the SLS print cooling phase. Note, dimensions are not to size. Adapted from [1].	8
Figure 4	Hysteresis of PA12 with indications of transition regions. Adapted from [1].	9
Figure 5	Hysteresis path during heating and intermediate cooling of a single layer of PA12. Adapted from [1].	10
Figure 6	Density hysteresis of PA12 during SLS printing.	11
Figure 7	Effect of cooling rate on the shrinkage of PA12 parts.	13
Figure 8	Schematic of a constitutive model of a viscoelastic material with strain hardening.	14
Figure 9	Schematic of a constitutive model of a viscoplastic material.	15
Figure 10	Temperature dependent Young's modulus of PA12.	16
Figure 11	Temperature dependent yield stress of PA12.	17
Figure 12	3.2 mm thick beam, oriented as simulated.	18
Figure 13	Bridge geometry.	18
Figure 14	Cross-sectional area along the build direction for the bridge.	20
Figure 15	Laser position over time along the build direction for the bridge.	21
Figure 16	Stair-step function for the beam with 4 lumped layers. Adapted from [1].	22
Figure 17	Sintering and contraction of a single particle in a layer. Note that the contraction of the particle itself and the contraction with respect to the previous layer are not to scale.	24
Figure 18	Sintering and contraction at near layer-completion. Note that the contraction of the particle itself and the contraction with respect to the previous layer are not to scale.	24

Figure 19	Overview of thermal and mechanical activation of each layer.	26
Figure 20	Full build-chamber geometry with beam at the center meshed with 3.2 mm element size. The beam is surrounded by loose powder at a coarser mesh size. The loose powder has a thickness of 24 mm below the beam and 4 mm above the beam.	27
Figure 21	Comparison of linear and quadratic shape functions [2].	28
Figure 22	Comparison of linear and quadratic mesh elements [2].	29
Figure 23	The Lisa X Printer.	31
Figure 24	Experimentally found temperature in the build chamber during the cooling phase.	32
Figure 25	The Keyence VR-3200 macroscope.	33
Figure 26	Illustration of the angle measured in the bridge curvature method. .	34
Figure 27	Temperature at the end of the heating phase sectioned in the xy-plane. The color legend represents temperature values, while the deformation of the geometry is visually included in the plot. Note that the x-axis has been stretched by a factor of 5 for visualization purposes, meaning the apparent deformation is also visually exaggerated by this factor.	35
Figure 28	Density at the end of the heating phase sectioned in the xy-direction. The color legend represents values of density, while the deformation of the geometry is visually included in the plot. Note that the x-axis has been stretched by a factor of 5 for visualization purposes, meaning the apparent deformation is also visually exaggerated by this factor.	36
Figure 29	Temperature in the heating phase at the center of each layer of a 4 layer beam.	37
Figure 30	Temperature in the heating phase in the 2nd layer of a 4 layer beam.	38
Figure 31	Density for each layer for 4 layer beam. Note that the point of transition from air to PA12 is marked in black for layers 2-4.	39
Figure 32	Temperature during heating and cooling phase for beam with 4 layers.	40
Figure 33	Stresses in the 1st layer pf beam with 4 layers, along with the yield stress.	41
Figure 34	Stresses in beam with 4 layers, along with the maximum and minimum yield stress reached during printing.	42

Figure 35	Viscoplastic strains in beam with 4 layers.	43
Figure 36	Strain components in beam with 4 layers for layer 2.	44
Figure 37	Warpage as a function of relative tolerance for: 3.2 mm mesh size, linear elements, 1 element per layer, 4 layers total.	45
Figure 38	Effect of element type for: relative tolerance 0.001, 1 element per layer, 4 layers total.	46
Figure 39	Effect of number of elements in build direction for: relative tolerance 0.001, 3.2 mm mesh size, linear elements, 4 layers total.	47
Figure 40	Effect of number of layers for: relative tolerance 0.001, appropriate mesh size, linear elements, 1 element per layer.	48
Figure 41	Temperature at the center of each layer in beam with 8 layers.	49
Figure 42	Position in build direction (x) at the end of the heating phase, for beam consisting of 8 layers. Position at the edge and the middle used to compute warpage is indicated on the figure. Note that the x -axis has been stretched by a factor of 5 for visualization purposes.	49
Figure 43	Density at the end of cooling of 8 layer beam. Note that the x -axis has been stretched by a factor of 5 for visualization purposes.	50
Figure 44	Strains in yy -direction at the end of the cooling phase, for 8 layer beam. Note that the x -axis has been stretched by a factor of 5 for visualization purposes.	50
Figure 45	Position in build direction at the end of the cooling phase, for 8 layers. Note that the x -axis has been stretched by a factor of 5 for visualization purposes.	51
Figure 46	Beam after removal of the cake.	51
Figure 47	Measuring the bend-direction of a beam in the macroscope.	52
Figure 48	Measurements for the first beam.	52
Figure 49	Strains in zz -direction and deformation at the end of the cooling phase, for 30 layer beam.	53
Figure 50	Picture of SLS printed bridge specimen.	54
Figure 51	Position in the build direction after cooling phase for 8 layer beam with double thickness. Note that the x -axis has been stretched by a factor of 5 for visualization purposes.	54

Figure 52	Position in the build direction after cooling phase for 8 layer beam with a laser power of 15.8 W. Note that the x -axis has been stretched by a factor of 5 for visualization purposes.	55
Figure 53	Measurements for the second beam	64
Figure 54	Measurements for the third beam	65
Figure 55	Measurements for the fourth beam	66
Figure 56	Thick beam 1 measurements.	67
Figure 57	Thick beam 2 measurements.	68

LIST OF TABLES

Table 1	Parameters used for the flash heating model	30
Table 2	Tabulated results of warpage.	53

NOMENCLATURE

Physics Constants

σ	Stefan-Boltzmann constant	$5.67 \times 10^{-8} \text{ W m}^{-2} \text{ K}^{-4}$
R	Universal gas constant	$8.314 \text{ J mol}^{-1} \text{ K}^{-1}$

Mechanical Symbols

$\dot{\lambda}_0$	Viscoplastic parameter	s^{-1}
$\dot{\lambda}_{vp}$	Viscoplastic multiplier	s^{-1}
$\dot{\varepsilon}$	Strain rate	s^{-1}
γ	Viscoplastic parameter	—
ν	Poisson's ratio	—
σ	Stress	Pa
σ_y	Yield stress	Pa
ε	Strain	—
E	Youngs' modulus	Pa
m	Viscoplastic parameter	—
p	Equivalent plastic strain	—
p_y	Viscoplastic parameter	—

Thermal Symbols

ϵ	Emissivity	—
ξ	Absorptivity	—
c_p	Specific heat capacity	$\text{J kg}^{-1} \text{ K}^{-1}$

h	Enthalpy	J kg^{-1}
h_{tc}	Heat transfer coefficient	$\text{W m}^{-2} \text{K}^{-1}$
k	Thermal conductivity	$\text{W m}^{-1} \text{K}^{-1}$
LH	Latent heat of fusion	J kg^{-1}
P	Power	W
q	Heat flux	W m^{-3}
T	Temperature	$^{\circ}\text{C}$

Other Symbols

δ	Layer height	μm
ϕ	Porosity	—
ρ	Density	kg m^{-3}
C	Courant number	—
H	Hatch spacing	mm
N_{ele}	Number of elements	—
t	Time	s
V	Velocity	m s^{-1}
CSA	Cross-sectional area	m^2

INTRODUCTION TO SELECTIVE LASER SINTERING (SLS)

1.1 SELECTIVE LASER SINTERING

Manufacturing is an important field in modern industries, as it lays the foundation for converting raw materials into the products we use in our everyday lives. Throughout history it has been necessary to continuously develop and improve manufacturing techniques to meet the growing demands, however, despite their many uses, traditional manufacturing methods such as machining, casting, and injection molding face, in some cases, significant limitations — especially when it comes to rapid prototyping or creating parts with complicated geometries. This is because the production of specialized parts often requires expensive tooling and molds. In industries where highly specialized parts are required, such as in the aerospace, automotive, or medical industry, the need for other manufacturing methods is, therefore, sometimes necessary [3]. Additive manufacturing (AM) is a method that can help solve some of these manufacturing problems, as with AM, you can make a part from a digital model, which grants you a lot of design freedom. In the diverse landscape of AM technologies, selective laser sintering (SLS) stands as a versatile and industrially relevant process. In Selective Laser Sintering (SLS), a laser selectively fuses polymer powder particles within a powder bed, enabling the production of strong parts with tight tolerances. Additionally, SLS doesn't need support structures like fused deposition modelling (FDM) does because the parts are surrounded by a "cake" of loose powder that holds the part in place while it prints. This makes it possible to make very complicated shapes like big undercuts or large bridging that would be impossible or too costly using traditional manufacturing methods. However, while SLS has some significant advantages, it does come with its own set of challenges, one of which is that the printed parts can be prone to warping. Localized heating followed by cooling happens very quickly in the laser sintering process, which leads to steep thermal gradients that can make the parts warp. To make high-quality SLS parts, especially when going from prototype to functional end-use components, you need to know how to control these effects, and thus, predictive tools that can anticipate these issues before printing can be very useful.

The Lisa X SLS printer, created by Sinterit, was used to manufacture every component in this thesis. The system consists of a powder bed, a laser source, galvo mirrors to guide the laser beam, a controlled build chamber, and a roller mechanism to apply powder layers one after the other. To lessen thermal gradients and warping, the build chamber is heated to a temperature that is just below the polymer material's melting point. From a digital model of the part, the galvo system directs the laser beam in SLS to selectively sinter specific areas of the powder bed.

The roller mechanism spreads a thin and uniform layer of powder (typically of height 0.075 - 0.175 mm) in the build area after each sintering pass [4, 5].

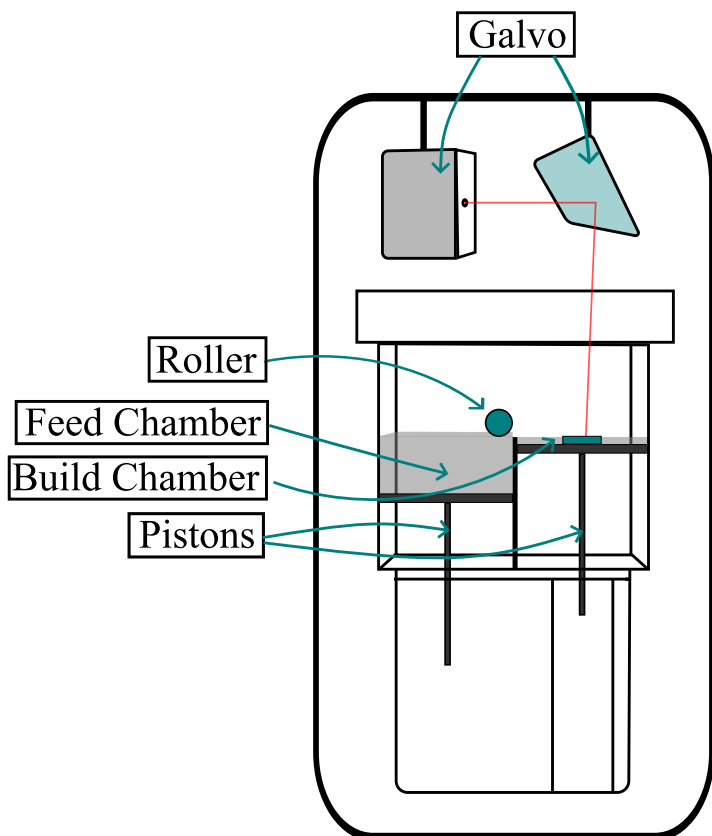


Figure 1: Schematic of the SLS printer and its components. Adapted from [1].

The Role of Simulations in SLS

When designing parts for SLS, numerical simulation can be a helpful tool for predicting warpage. Engineers can anticipate possible problems and optimize the part design or process parameters before printing by using the simulation to model the mechanical and thermal behavior of a part during the printing process. The SLS process can be modelled in several ways [6]:

- **Laser scan path simulation** — By simulating the laser's scanning path, this technique records localized in-build-plane heating effects. Although this method yields the most

detailed results, it is also computationally costly, particularly for large or intricate parts.

- **Flash heating** — In this method, an entire layer is heated evenly at the same time. This simulation reduces the time significantly because no scanning path is modelled, but it doesn't capture the in-build-plane effects and thus catches the "bulk" warpage only.
- **Sequential flash heating** — This method divides each layer into strips and applies the heat source to each strip in turn. This method strikes a balance between accuracy and computational efficiency.

Compared to experimental approaches, simulations have certain advantages and disadvantages. They enable rapid changes to part design, process parameters, and material models without the cost or time associated with physical printing. The simulation also allows for the view of internal phenomena, such as internal stresses or temperature gradients, which are difficult to measure experimentally. Nevertheless, simulations depend on input data, including material properties and boundary conditions, as well as assumptions and simplifications. The simulation results could differ greatly from actual behavior if these are erroneous. Consequently, experimental validation is still a valuable part of any workflow based on simulation.

Research Objectives

The viability of simulating the thermal development and internal strains brought on by densification during selective laser sintering using a flash heating model is investigated in this work. The model accounts for the various temperature-dependent material properties, the viscoplastic effects, and the strains caused by changes in density, as this type of shrinkage-induced deformation can lead to warpage. The model's predictions and experimental findings will be compared in order to validate it.

The study expands on earlier SLS process simulation research. **Riedlbauer et al.** [7] used experiments and numerical analysis to investigate melt pool formation in single-line SLS printing. **Zhang et al.** [8] developed an in-house software that uses parallel computing and adaptive meshing to model SLS multi-track prints. **Bayat et al.** [6] investigated SLM components with both a flash heating and a sequential flash heating thermomechanical approach. **Shen et al.** [9] modelled the temperature, crystallization, viscoplasticity, and residual stress in SLS printing of PA12. **Li et al.** [10] created a numerical model of

SLS-printed PA12 parts and validated their results experimentally. Their model includes the thermal, recrystallization, and viscoplastic strains, and they have a focus on shrinkage and warpage. **Teo et al.** [11] investigated the recrystallization in depth experimentally and found a relation between cooling rate and shrinkage. **Issametova et al.** [12] used the bridge curvature method to analyze residual stresses in 3D-printed polymer parts. The objective is to create an easy-to-use and efficient method of computing warpage in SLS-printed parts. By combining simulation with experimental verification, this work seeks to provide a framework that can be used to improve the print process of SLS-printed components with regard to process efficiency, dimensional accuracy, and mechanical performance.

MODELLING FRAMEWORK

The mechanical analysis and the thermodynamics during SLS are complex and governed by several fundamental equations and, importantly, the boundary conditions. This section delves into these equations, elucidating the associated boundary conditions during the heating and the cooling phases, and explores the temperature-dependent properties of the materials used for SLS printing.

2.1 MATERIALS IN SLS-PRINTING

Thermoplastics and thermosets are the two major subcategories of polymers. Of these two, only thermoplastics are suitable for SLS printing, since thermoplastics melt when exposed to elevated temperatures, as opposed to thermosets, which degrade instead. Thermoplastics can be further categorized depending on their crystallinity. Amorphous thermoplastics are thermoplastics with a random molecular structure. Amorphous polymers do not have a sharply defined melting point, instead, they melt over a wider range. This is a problem in SLS printing, as we want to be able to raise the temperature just enough for it to sinter at the right time without thoroughly melting. For this reason, semi-crystalline thermoplastics are used instead, as semi-crystalline thermoplastics have regions of ordered crystal structure, which results in a well-defined melting point. The powder used in this work is the semi-crystalline thermoplastic called polyamide 12, PA12 for short [13].

2.2 THERMAL MODELLING

The thermal behavior in SLS is governed by the heat conduction equation, which accounts for the distribution and flow of heat within a material [14]:

$$\frac{\partial}{\partial x} \left(k \frac{\partial T}{\partial x} \right) + \frac{\partial}{\partial y} \left(k \frac{\partial T}{\partial y} \right) + \frac{\partial}{\partial z} \left(k \frac{\partial T}{\partial z} \right) + q_v = \rho c_p \frac{\partial T}{\partial t} \quad (1)$$

Where:

- T is the temperature.
- k is the thermal conductivity of the material.
- q_V is a volumetric heat source, which in this case corresponds to the laser energy input.
- ρ is the material density.
- c_p is the specific heat capacity.

Heat flux due to conduction is given by Fourier's law [14]:

$$q_{\text{cond}} = -k \frac{dT}{dx} \quad (2)$$

As such, the first three terms on the left-hand side of Eq. 1 represent the rate of heat conduction in each direction x , y and z . Thus, Eq. 1 encapsulates the balance between the applied heat source, the rate of heat conduction, and the temporal change of temperature within the material.

2.2.1 Thermal Boundary Conditions in the SLS Process

The thermal boundary conditions in SLS include convection and radiation:

- **Convection:** The convective heat flux at a surface is [14]:

$$q_{\text{conv}} = h_{\text{tc}}(T_s - T_\infty) \quad (3)$$

Where h_{tc} is the heat transfer coefficient, T_s is the surface temperature, and T_∞ is the ambient temperature.

- **Radiation:** Radiative heat flux is expressed as [14]:

$$q_{\text{rad}} = \epsilon \sigma(T_s^4 - T_\infty^4) \quad (4)$$

Here, ϵ is the emissivity of the surface, and σ is the Stefan-Boltzmann constant.

The thermal boundary conditions are crucial for accurately modelling the thermal environment during SLS. They define the thermal behavior at the interfaces of the material and its

surroundings. In this case, the model is split up into a heating phase and a cooling phase since the boundary conditions change once the printer is turned off and allowed to cool.

Heating Phase

Fig. 2 illustrates the thermal boundary conditions during the heating phase. In the heating phase, just a small section of the total build volume is considered.

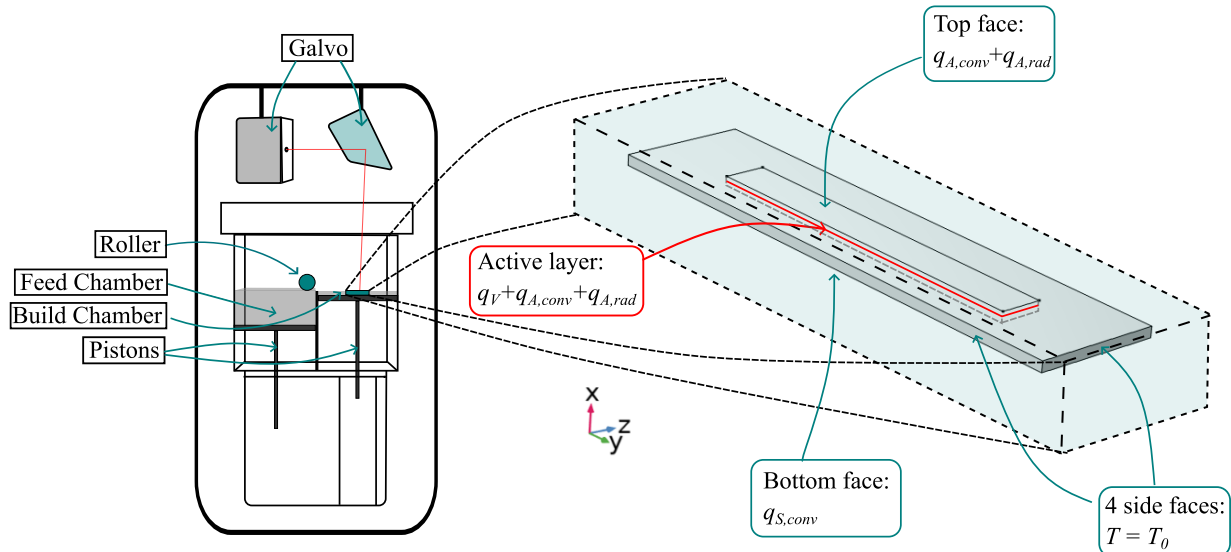


Figure 2: Illustration of the SLS printer and the boundary conditions during the heating phase. Note, dimensions are not to size. Adapted from [1].

- **Bottom Face:** An artificial convection boundary condition is applied to simulate heat conduction through the base of the build chamber. Studies have determined an effective heat transfer coefficient of approximately $10 \text{ W m}^{-2} \text{ K}^{-1}$ for similar SLS systems [15]. The ambient temperature in the heating phase is observed during printing to be $T_\infty = 175^\circ\text{C}$.
- **Side Faces:** These are subjected to Dirichlet boundary conditions, maintaining the temperature at the initial powder temperature, $T_0 = 175^\circ\text{C}$. This assumption holds only when the simulated build volume is sufficiently large, such that the heating from the laser doesn't affect the temperature at the edges.
- **Top Face and Active Layer:** Both convection and radiation boundary conditions are considered. The convective heat transfer coefficient with the ambient air is $15 \text{ W m}^{-2} \text{ K}^{-1}$ [16], and the emissivity of the material surface is 0.8 [17]. Additionally, the active layer also has the volumetric heat source of the laser applied.

Cooling Phase

Fig. 2 illustrates the thermal boundary conditions during the cooling phase, where the entire build volume (150 mm x 200 mm in the zy-plane) is considered.

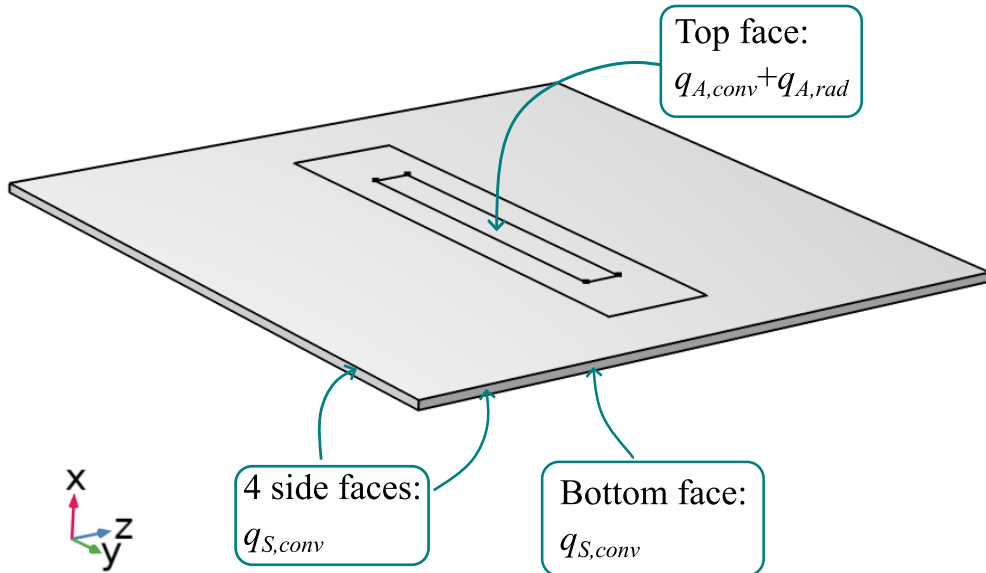


Figure 3: Boundary conditions during the SLS print cooling phase. Note, dimensions are not to size. Adapted from [1].

During cooling, the top face has the same boundary condition of combined convective and radiative heat losses, the bottom face maintains the artificial convection boundary condition, and since the simulated build volume is expanded to the size of the true build volume, the side faces are now in contact with the build chamber wall, and as such, the side faces also get the same artificial convection boundary condition. The same heat transfer coefficients and emissivity values as in the heating phase are applied to model the cooling behavior accurately, however, the ambient temperature is different. To determine the ambient temperature in the cooling phase, the temperature within the build chamber can be logged experimentally.

2.2.2 Thermal Properties of PA12

Thermal hysteresis refers to the phenomenon where a material exhibits different heating and cooling paths in terms of its thermal properties. This behavior occurs with regard to enthalpy during the SLS process, and in this work the enthalpy function is defined as [18]:

$$h(T) = C_{p0} \cdot T + LH \cdot \text{step}(T - T_m) \quad (5)$$

Here $C_{p0} = 2 \text{ J g}^{-1} \text{ K}^{-1}$ is the specific heat capacity of the solid phase, $LH = 145 \text{ J g}^{-1}$ is the latent heat of fusion, T_m is the melting temperature of 186.2°C , and step is a smoothed step function that adds in the latent heat once the temperature reaches the melting region [16]. The enthalpy curve is illustrated in Fig. 4.

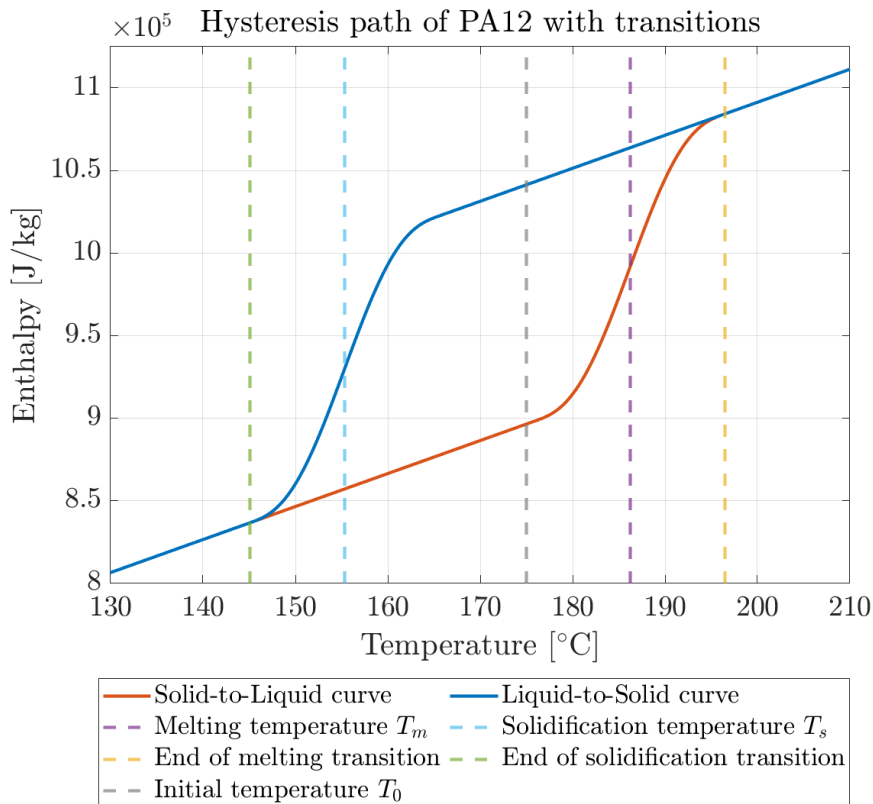


Figure 4: Hysteresis of PA12 with indications of transition regions. Adapted from [1].

Additionally, to model this, the PA12 initially follows the solid-to-liquid curve in Fig. 4 as it is heated. Once the maximum temperature is reached and the material begins to cool, it then transitions along the liquid-to-solid curve. However, if the heating did not progress all the way to the end of the melting transition, the material may not fully align with the standard liquid-to-solid path. Therefore, to ensure continuity and consistency in

the hysteresis behavior, the liquid-to-solid curve must be shifted to start from the actual maximum temperature reached during heating.

The actual behavior of the enthalpy during the SLS process is shown in Fig. 5. The powder starts at $T_0 = 175^\circ\text{C}$ at point 1. Then it gets heated to approximately the melting temperature at point 2. Then it cools down, following a scaled-down version of the liquid-to-solid curve to point 3. As layers above get added and heated, the layers beneath will receive some indirect heat, causing an enthalpy increase from point 3 to point 4, and then back to point 5 once the heating stops.

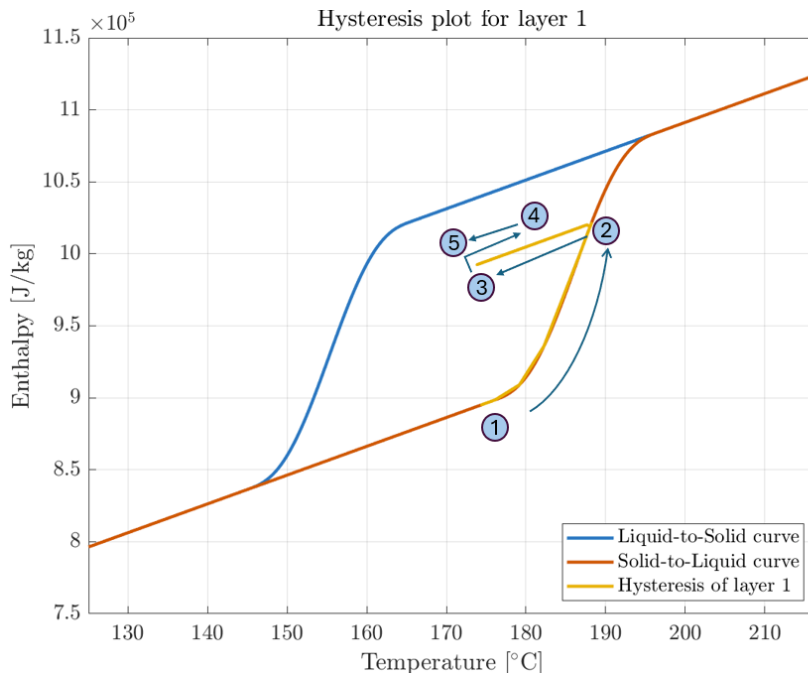


Figure 5: Hysteresis path during heating and intermediate cooling of a single layer of PA12.
Adapted from [1].

The enthalpy is related to the specific heat capacity using the following expression [19]:

$$dh = c_p(T) dT \quad (6)$$

Another occurrence of hysteresis occurs with the density of PA12 during printing. The density is determined through the data depicted in Fig. 6 [9].

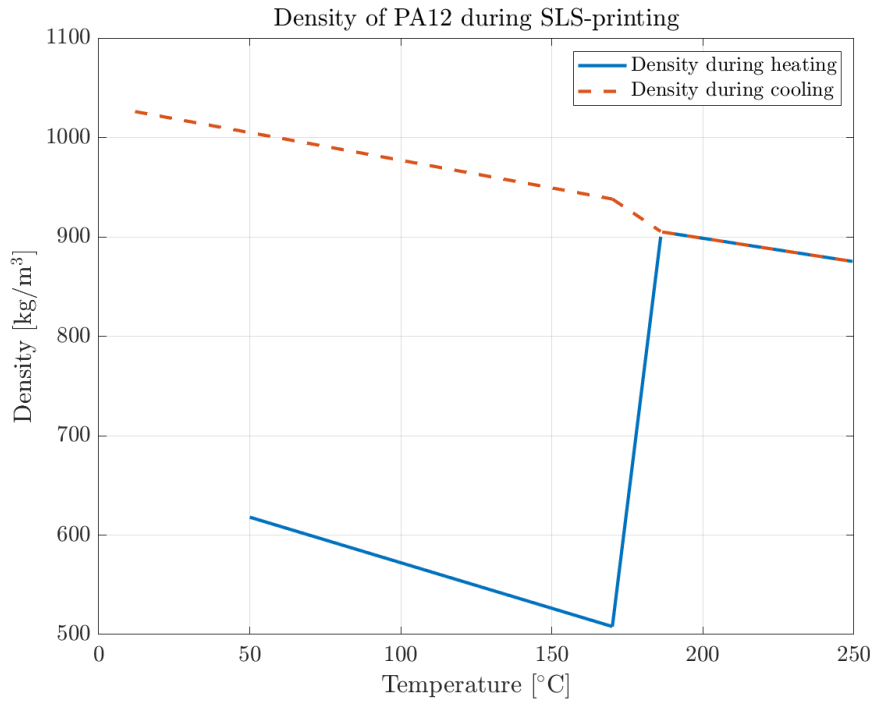


Figure 6: Density hysteresis of PA12 during SLS printing.

In Fig. 6 it can be seen that during heating, when PA12 is a powder, the density is quite low due to high porosity. Once the PA12 is sintered, the air pockets between the powder particles get replaced with solid material, leading to a rapid increase in density as solidification occurs (at about 170 °C). During cooling, the material densifies further. Thus, PA12 follows different density paths depending on whether it has undergone a transition from powder to solid or not.

The thermal conductivity is modelled to be dependent on the density through the porosity [20]:

$$k_{\text{powder}}(\phi) = k_{\text{solid}}(1 - \phi) \quad (7)$$

Where the porosity ϕ relates to the material density as [21]:

$$\phi(\rho) = \frac{\rho_{\text{solid}} - \rho}{\rho_{\text{solid}}} \quad (8)$$

These relationships highlight that as density increases, the thermal conductivity increases, affecting heat transfer within the powder bed.

2.3 MODELLING OF THE SOLID MECHANICS

The static equilibrium condition governs the solid mechanics modeling in COMSOL [22]:

$$\nabla \cdot \mathbf{S} + \mathbf{f}_V = 0 \quad (9)$$

It states that the divergence of the stress tensor plus any external body forces must sum to zero, assuming inertia is negligible.

The stress tensor consists of both elastic and inelastic stresses, with corresponding strains:

$$\boldsymbol{\varepsilon} = \boldsymbol{\varepsilon}_{el} + \boldsymbol{\varepsilon}_{inel} \quad (10)$$

Where the total strains are the symmetric part of the displacement gradient, assuming small displacements [22]:

$$\boldsymbol{\varepsilon} = \frac{1}{2} \left[(\nabla \mathbf{u})^T + \nabla \mathbf{u} \right] \quad (11)$$

In this work the total strain consists of the following components:

$$\boldsymbol{\varepsilon} = \boldsymbol{\varepsilon}_{el} + \boldsymbol{\varepsilon}_{vp} + \boldsymbol{\varepsilon}_{ext} \quad (12)$$

Which corresponds to the elastic strains, the viscoplastic strains, and the external strains. In this case the external strains are the thermal and crystallization-induced strains, which are the strains caused by changes in density in SLS. For this reason, the volumetric external strains are modelled as in Eq. 13:

$$\boldsymbol{\varepsilon}_{ext} = \frac{\rho(T_{ref})}{\rho(T)} - 1 \quad (13)$$

Note that this means that the external strains in each of the three principal directions (x , y , and z) are each a third of Eq. 13. The reference temperature, T_{ref} , is chosen as the temperature at the point of activation, which is the point just before the next layer gets activated. This will be explained more in-depth in section 3.2.

Additionally, an important effect to consider for accurately capturing densification is the influence of cooling rate on shrinkage. Fig. 7 shows the experimentally observed shrinkage as a function of cooling rate [11].

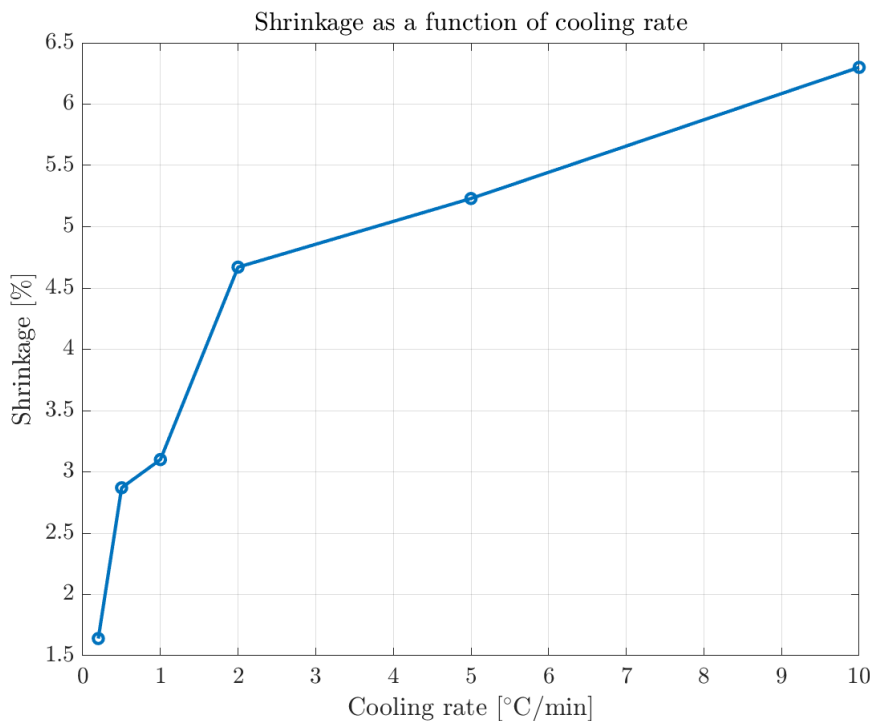


Figure 7: Effect of cooling rate on the shrinkage of PA12 parts.

This data can be used to adjust the density function shown in Fig. 6 during cooling in order to predict the correct shrinkage for each layer.

However, it is important to note that the cooling-rate-dependent densification arises primarily due to recrystallization. According to [9], recrystallization occurs at around ~ 150 °C, meaning that the cooling rate affects shrinkage only up to this temperature. Below this point, the shrinkage is effectively “locked” in.

2.3.1 Viscoplasticity

When working with viscoplasticity, it is common to schematically represent the constitutive system with branches consisting of springs, dashpots, and sliders.

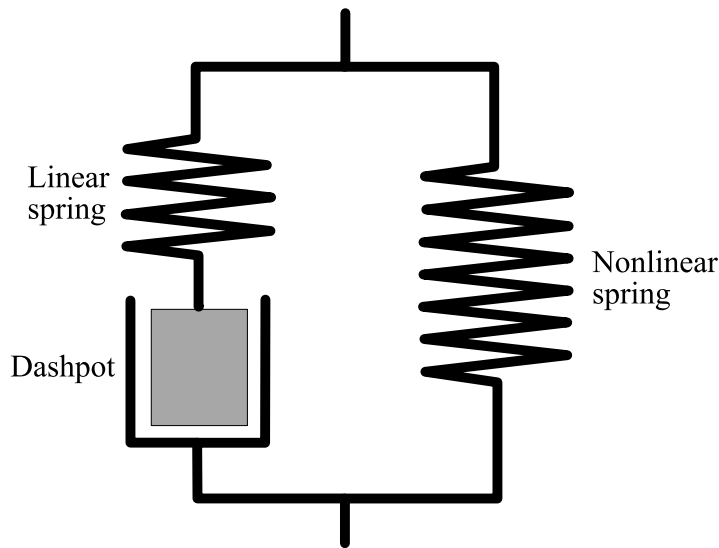


Figure 8: Schematic of a constitutive model of a viscoelastic material with strain hardening.

Fig. 8 shows a common system of how a viscoelastic thermoplastic can be described by the deformation of two parallel branches. The left branch, which is also known as Maxwell's viscoelastic model, consists of a linear spring that represents the elastic response and a dashpot that represents the temperature- and strain-rate-dependent viscoelasticity. Viscoelasticity means that the material exhibits strain-rate-dependent, reversible deformation below the yield stress of the material, whereas viscoplasticity means that the material exhibits strain-rate-dependent, permanent deformation only above the yield stress. The right branch is a nonlinear spring that corresponds to the deformation due to strain hardening at large strains. For our purposes, however, the strain hardening branch is neglected as the strains are generally too small for it to matter [9]. Additionally, we are mostly interested in the viscoplasticity that occurs as the PA12 is sintered, as, at the point of sintering, the yield stress, which is temperature-dependent, is very low, which makes viscoplasticity prevalent. To schematically represent viscoplasticity instead of viscoelasticity, Maxwell's model can be replaced by a "Bingham-type" model, which consists of a spring in series with a dashpot and a plastic slider in parallel. The plastic slider is activated once the yield stress is exceeded, allowing the dashpot to move, see Fig. 9 [23].

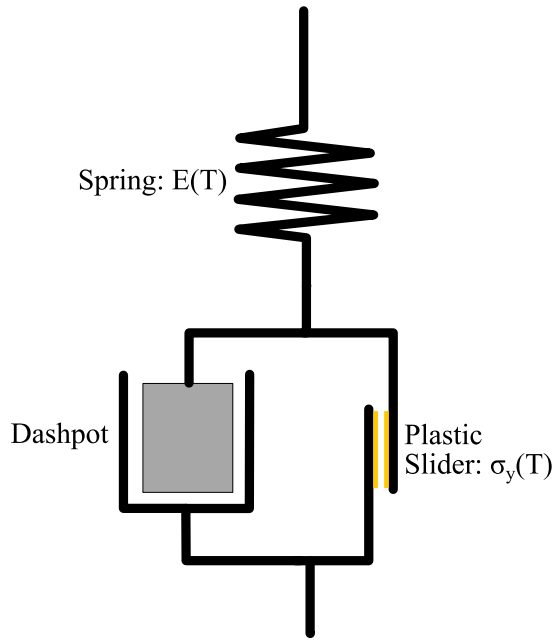


Figure 9: Schematic of a constitutive model of a viscoplastic material.

The viscoplastic strain rate is:

$$\dot{\epsilon}_{vp} = \dot{\lambda}_{vp} \frac{\partial f}{\partial \sigma} \quad (14)$$

Where $\dot{\lambda}_{vp}$ is called the viscoplastic multiplier, and $\frac{\partial f}{\partial \sigma}$ is the gradient of the yield function with respect to the stress tensor σ . The yield function is used to determine whether the yield stress is exceeded:

$$f = \sqrt{3s : s/2} - \sigma_y(T). \quad (15)$$

Where $\sigma_y(T)$ is the temperature-dependent yield stress. Using Eq. 15 and the chain rule to rewrite Eq. 14 yields:

$$\dot{\epsilon}_{vp} = \dot{\lambda}_{vp} \frac{3s}{2\sqrt{3s : s/2}} \quad (16)$$

The viscoplastic multiplier is expressed by [6]:

$$\dot{\lambda}_{vp} = \dot{\lambda}_0 \left(\frac{\sqrt{3s : s/2}}{\sigma_y(T)(1 + \gamma - \gamma \exp(-p/p_y))} \right)^m \quad (17)$$

Where $\dot{\lambda}_0$, m , γ , and p_y are viscoplastic parameters from [6]. Additionally, the equivalent plastic strain p is:

$$p = \sqrt{2\epsilon_{vp} : \epsilon_{vp}/3} \quad (18)$$

2.3.2 Mechanical Boundary Conditions in the SLS Process

Contrary to other additive manufacturing methods, in SLS printing, the beam is not fixed to the build plate. As such, the beam should be able to warp freely. However, COMSOL requires at least one fixed boundary to ensure numerical stability and avoid rigid body motion. For this reason, some powder beneath the beam is present and modelled. Thus, in this work, the powder is fixed at the bottom surface, reminiscent of a "no-slip condition", but as the powder has no stiffness, it doesn't prevent the beam from warping freely.

2.3.3 Mechanical Properties of PA12

To model the solid mechanics, the Young's modulus and Poisson's ratio are needed for the elasticity matrix. The Poisson's ratio is assumed to be constant at 0.4 [9], and the Young's modulus is temperature-dependent and depicted in Fig. 10 [10].

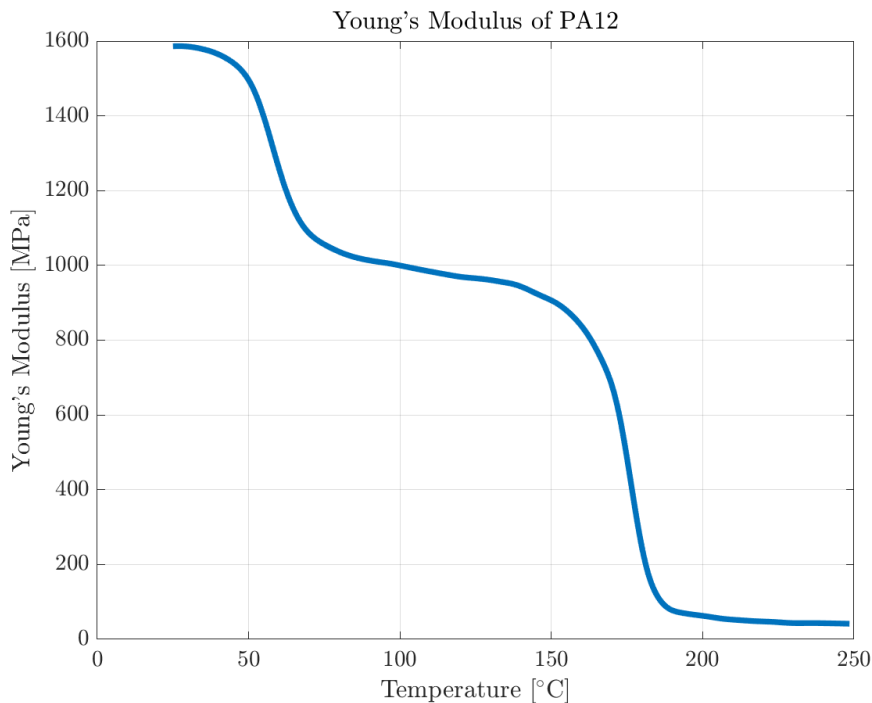


Figure 10: Temperature dependent Young's modulus of PA12.

Additionally, the yield stress is needed to determine when the viscoplasticity applies. The yield stress is heavily temperature-dependent, and thus it can be easily exceeded near the melting point. The yield stress as a function of temperature is shown in Fig. 11 [10]:

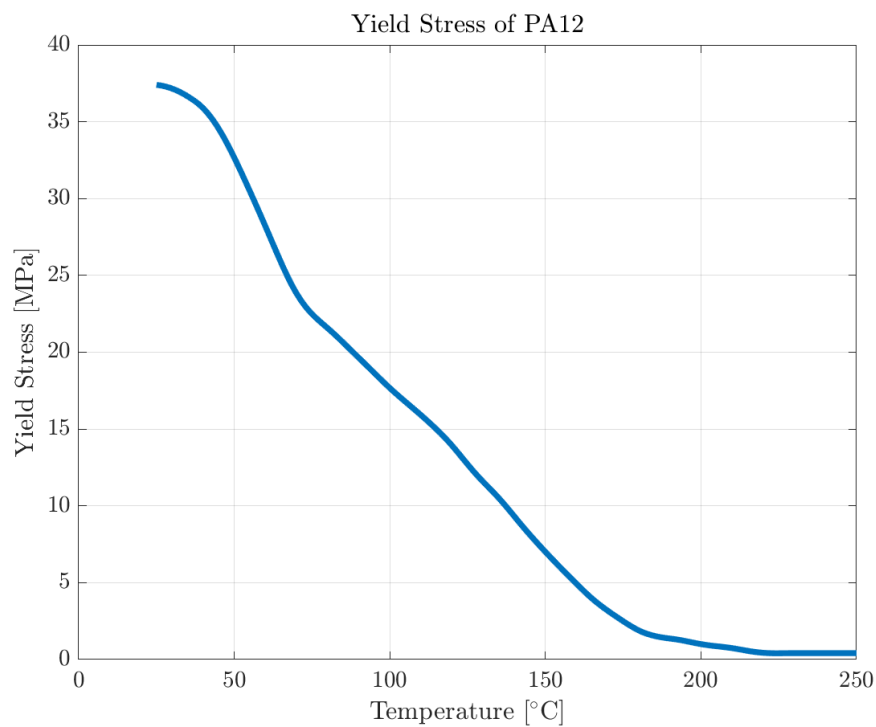


Figure 11: Temperature dependent yield stress of PA12.

SIMULATION CONSIDERATIONS

3.1 FLASH HEATING SIMULATION

This section describes the implementation of a flash heating model, developed in COMSOL, to model heat input during sintering of both a beam (Fig. 12) and a bridge-shaped part (Fig. 13).

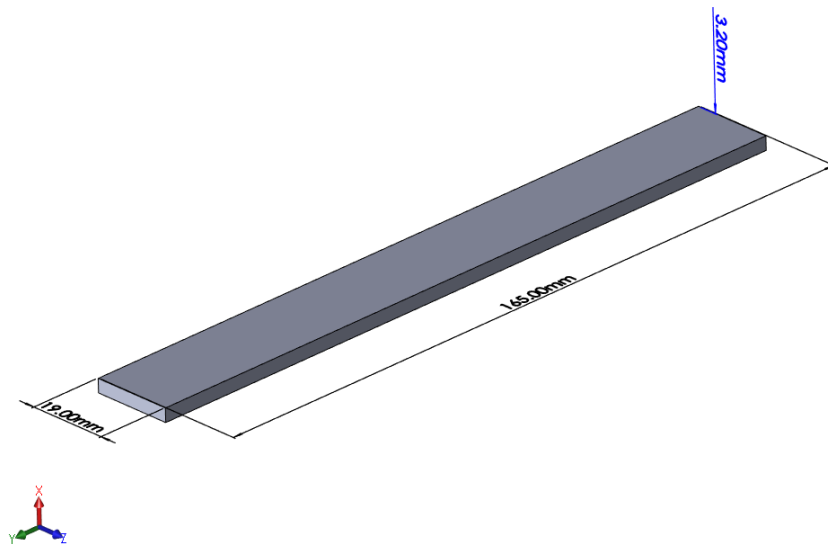


Figure 12: 3.2 mm thick beam, oriented as simulated.

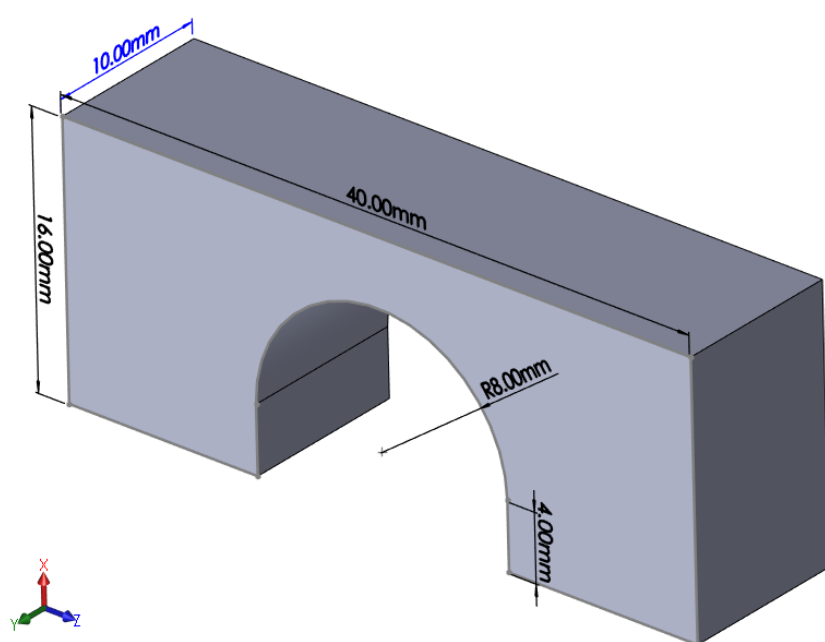


Figure 13: Bridge geometry.

3.1.1 Volumetric Heat Source

In contrast to other work, which often uses a Gaussian laser distribution to model a moving heat source, this model applies the laser energy as a uniform volumetric heat source over an entire layer. The method is called flash heating, and the governing expression is [6]:

$$q_v = \frac{\xi P}{H V_{\text{scan}} t_{\text{heat}} \delta} \quad (19)$$

Where P is the laser power, $\delta = 100 \mu\text{m}$ is chosen to be the layer thickness, $V_{\text{scan}} = 1.1 \text{ m s}^{-1}$ [16] is the laser scanning speed for the Lisa-X printer, $\xi = 0.4$ is the absorptivity for PA12 [17], and $H = 0.36 \text{ mm}$ is the selected hatch spacing for the Lisa-X printer. The exposure time per layer, t_{heat} , can be determined by simulating the duration for which a point is exposed to heat as a laser, moving at a velocity V_{scan} , passes over it. The exposure time is found to be $t_{\text{heat}} = 0.0012 \text{ s}$.

The Lisa-X SLS printer has a maximum power output of $P_{\text{max}} = 15.8 \text{ W}$, but for standard operation, the power is reduced using an energy scaling factor of 0.45 [16]:

$$P = 0.45 \cdot 15.8 \text{ W} = 7.11 \text{ W} \quad (20)$$

For the flash heating implemented in this work, not only is every layer uniformly heated, but multiple layers get grouped into a single “lumped” layer that is heated as a unit. This decreases the fidelity of the model but saves computation time. The number of layers in a lumped layer is one of the parameters that will be necessary to investigate the effects of. An issue that occurs with lumped layers is that within every lumped layer, a through-build-direction temperature gradient develops since the lumped layer is bounded by air at the top and PA12 powder below. In selective laser sintering, however, it is reasonable to assume that within a single lumped layer, particles at the same build-plane location, but at different heights, experience similar thermal histories. As such, the temperature is averaged just along the build direction across the lumped layer.

3.1.2 Laser Movement Along Build Direction

Controlling the laser's motion in the build direction is critical to accurate heat modelling. In this setup, the build direction is defined as the x -axis. The laser moves in discrete steps rather than continuously, thus mimicking real build behavior.

The first step is to determine the cross-sectional area of the part along the x -axis. For the beam geometry, Fig. 12, this is constant, but for the bridge, the area varies and must be treated as a function of position in the build direction: $\text{CSA}(x)$. To compute $\text{CSA}(x)$, the part is sliced at regular intervals along x , and cross-sectional areas are interpolated between slices:

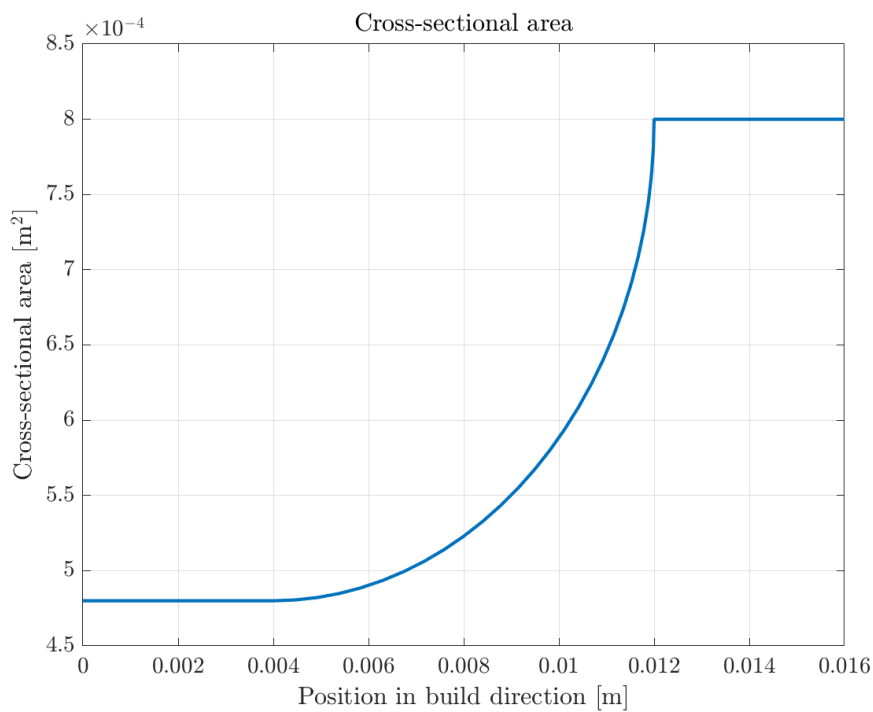


Figure 14: Cross-sectional area along the build direction for the bridge.

Using this cross-sectional profile, the laser velocity at each position x is defined by:

$$V_x(x) = \frac{\delta \cdot V_{\text{scan}} \cdot H}{\text{CSA}(x)} \quad (21)$$

The position of the laser over time is then governed by:

$$\frac{dx}{dt} = V_x(x) \quad (22)$$

This equation is solved in COMSOL using an ODE solver to determine the laser position as a function of time, $x(t)$. Using Eq. 22 and knowing by experimental measurement that

the time in between layer depositions is ~ 25 s, the total time of the heating phase can be computed, and Fig. 15 can be created:

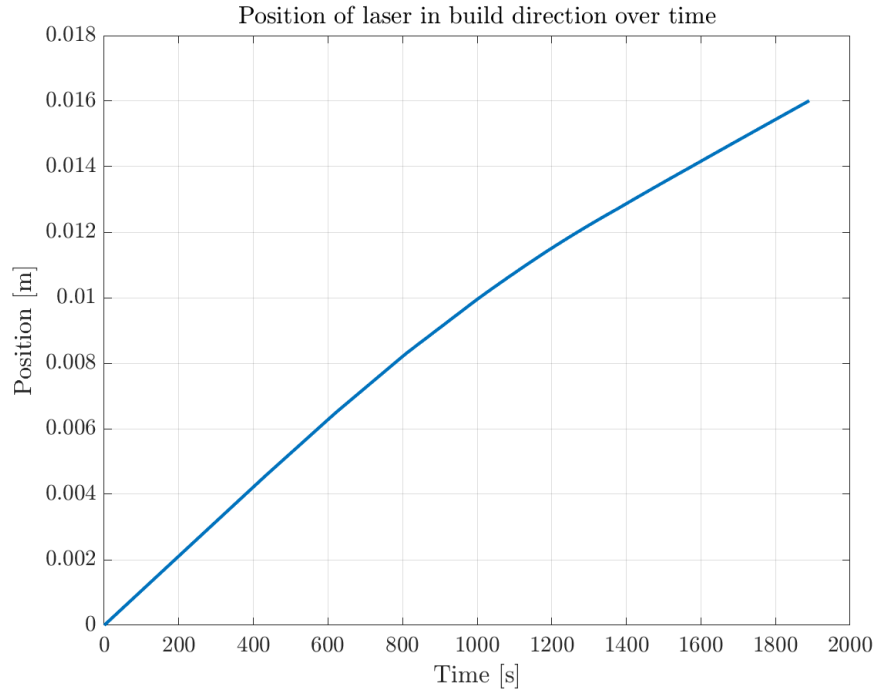


Figure 15: Laser position over time along the build direction for the bridge.

Fig. 15 shows that for the bridge, the position of the laser in the build direction increases more rapidly in the beginning than at the end, since the cross-sectional area is the smallest initially and increases towards the end.

Although $x(t)$ is continuous, laser motion in the real process occurs layer-by-layer. To capture this behavior, $x(t)$ is passed through a stair-step function that floors the position between discrete intervals of the layer height, δ . This results in a stepped motion consistent with layer-based printing:

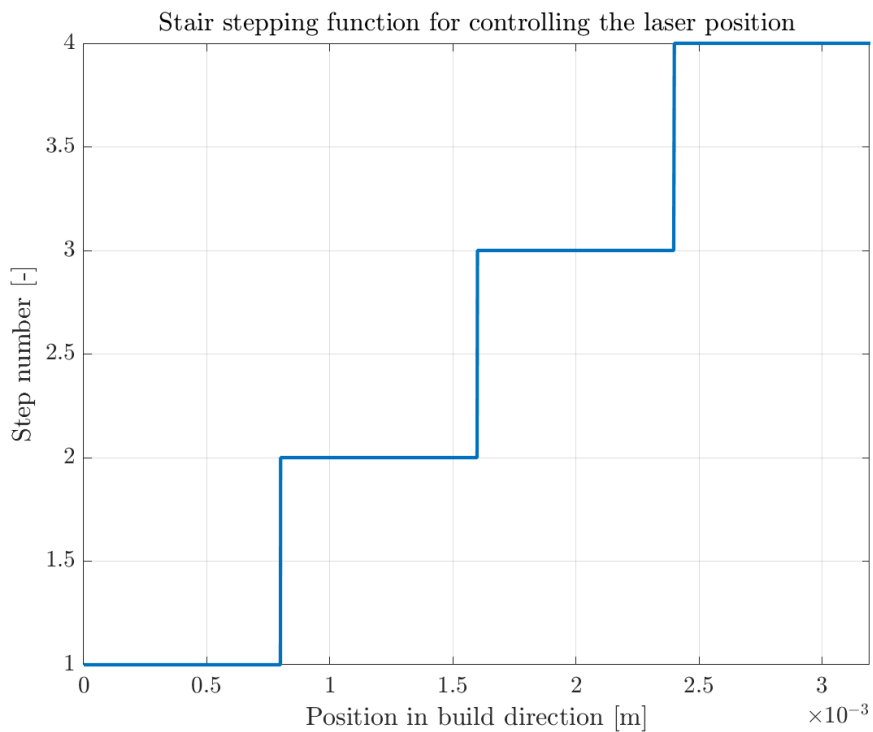


Figure 16: Stair-step function for the beam with 4 lumped layers. Adapted from [1].

The stair function is then used to accurately control the placement of the heat source over time in the simulation.

3.2 ACTIVATION

As the layers get flash heated, it is important that the layers get thermally and mechanically activated in an appropriate manner. Here, thermally active layers are any previously heated layers as well as the layer currently being heated, and the deactivated layers are any layers yet to be heated. With regard to thermal activation, the first thing to address is how to properly define the thermal properties of active and deactivated layers. The active layers have the thermal properties of PA12, whereas the deactivated layers have the thermal properties of air. However, having the deactivated layers have the thermal properties of air presents an issue because the deactivated layers will start to heat up. This is a problem, as when the time comes for this layer to be activated and the thermal properties will shift to PA12, the initial temperature will be above that of the initial temperature of newly deposited powder of 175 °C. For this reason, just before activation, a volumetric heat sink is applied to the deactivated layer using a convection expression as in Eq. 3, with the ambient temperature

set to 175 °C. The heat transfer coefficient is chosen to be sufficiently high to ensure that the temperature of the deactivated layer reaches 175 °C before it becomes active.

What activates a layer mechanically is whether or not the external strains and viscoplastic strains apply and whether a layer's elasticity matrix has an activation scale factor of 1e-10 applied. The activation scale factor ensures that any mechanically inactive layers have no effect on the active layers. This behavior can be implemented using COMSOL's built-in activation feature. The mechanical activation logic is slightly different than the thermal activation logic, and Fig. 19 illustrates the logic behind both the thermal and mechanical activation for a 4-layer example. The mechanical activation logic in this thesis is based on the assumption that an entire layer needs to be fully sintered before it is mechanically active. The logic behind this assumption stems from the idea that as the laser scans a layer, any contraction of individual particles due to the rapid increase in density only has a local effect and doesn't affect any previously sintered layers in a significant "bulk" manner. Fig. 17 illustrates this idea, as in a true, scanning-path SLS print it is unreasonable to think that the very first particles to be sintered have any significant effect on the previously sintered layers that would cause the previous layers to want to warp. If we were to assume that the currently heated layer is mechanically active in a flash heating model, it would be as if the entire layer contracts at once at the moment of heating, resulting in a large influence on the layers below, vastly overestimating the effect that the contraction of individual particles in a true scanning-path SLS print has on the layers below.

As the true scanning-path SLS print continues, the initially sintered particles have cooled back down and are reaching the end of their contraction. The initially sintered particle's contribution to affecting the layers below becomes larger as the layer grows in size but smaller as the contraction nears its end. As such, the recently sintered particles near the end have a larger effect on the previous layers, as they are part of a larger layer throughout their whole lifetime and have only just begun their contraction. In general, the overall effect of contraction of particles on the layers below becomes larger as the layer grows in size, as in Fig. 18. This also means that in a true scanning-path SLS print, there *is* an effect on warpage during heating that is smaller than the effect of applying flash heating during heating but larger than the effect of not applying flash heating during heating. This is one of the limitations of flash heating, and since in this work it is chosen to not apply flash heating during heating, we would expect this flash heating setup to slightly underestimate the warpage.

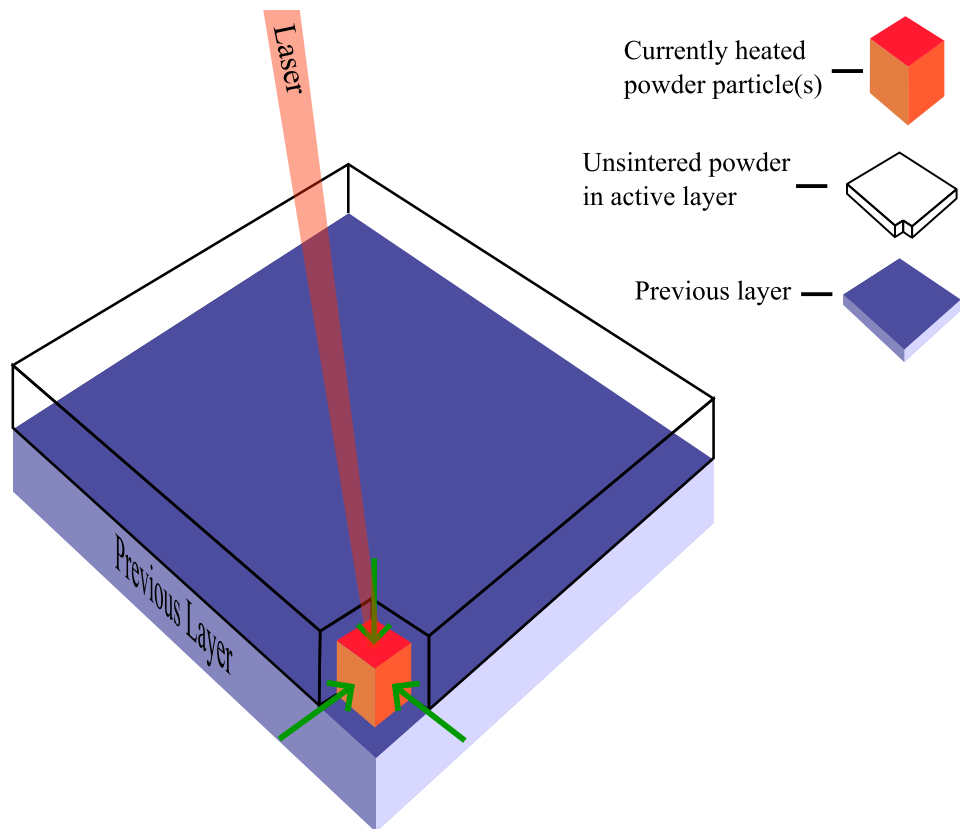


Figure 17: Sintering and contraction of a single particle in a layer. Note that the contraction of the particle itself and the contraction with respect to the previous layer are not to scale.

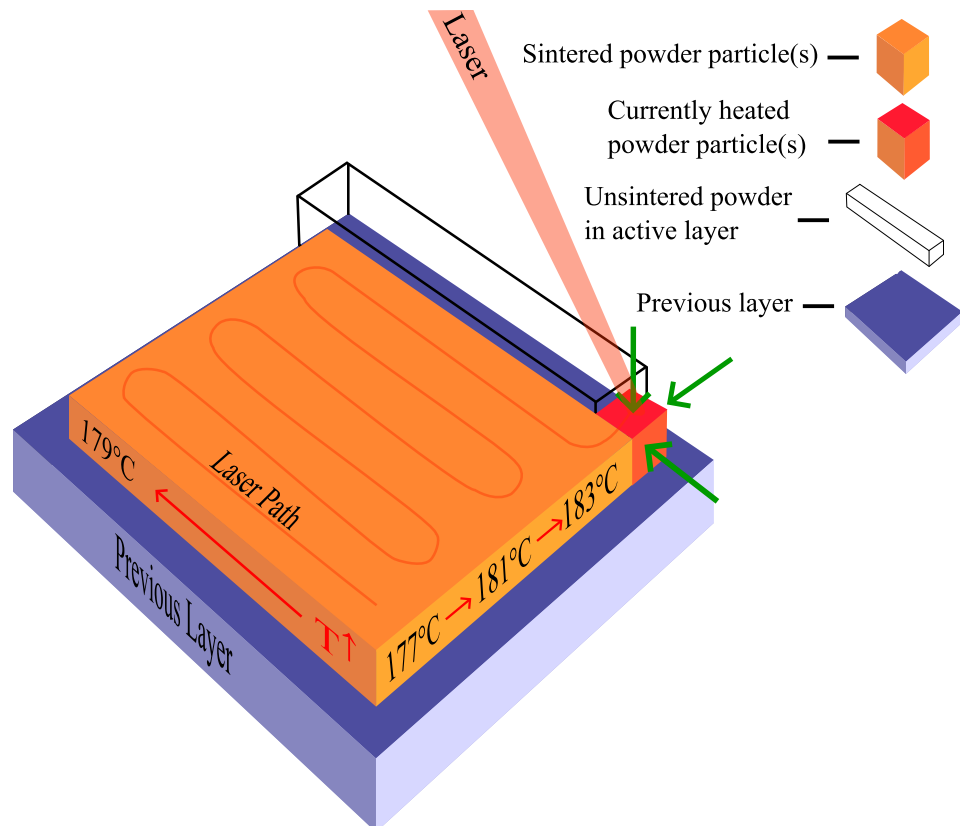
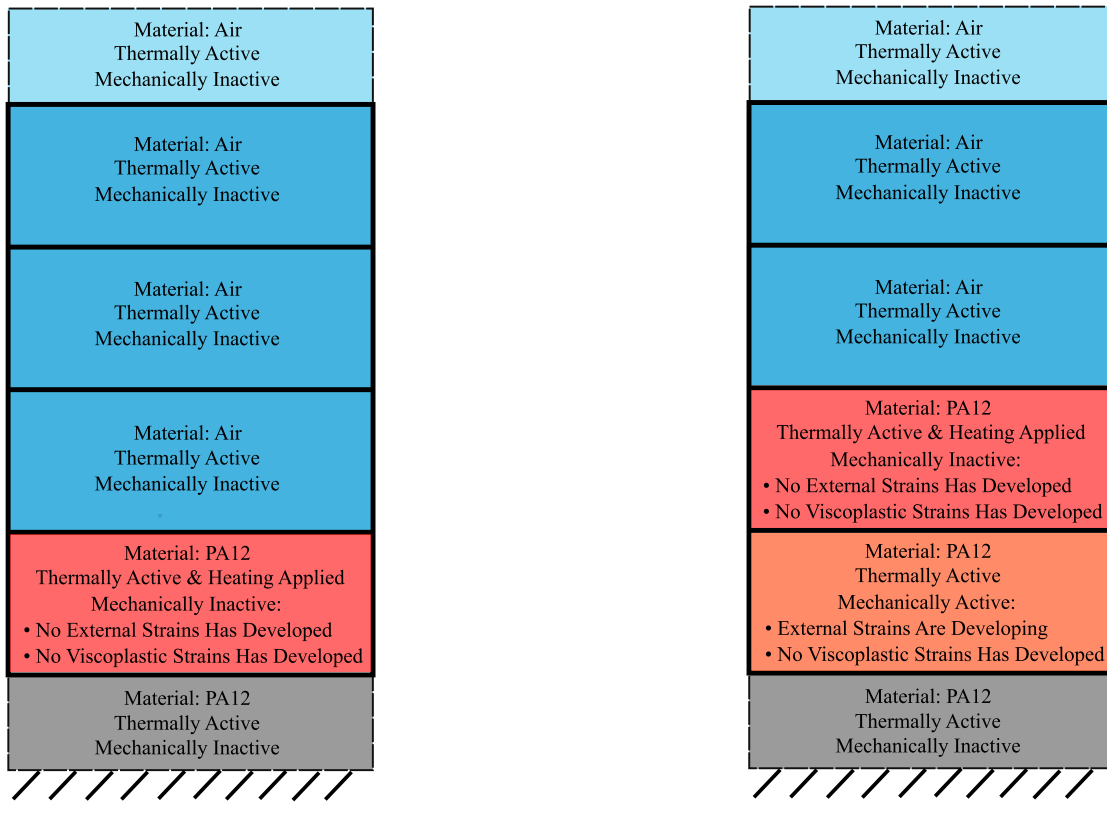


Figure 18: Sintering and contraction at near layer-completion. Note that the contraction of the particle itself and the contraction with respect to the previous layer are not to scale.

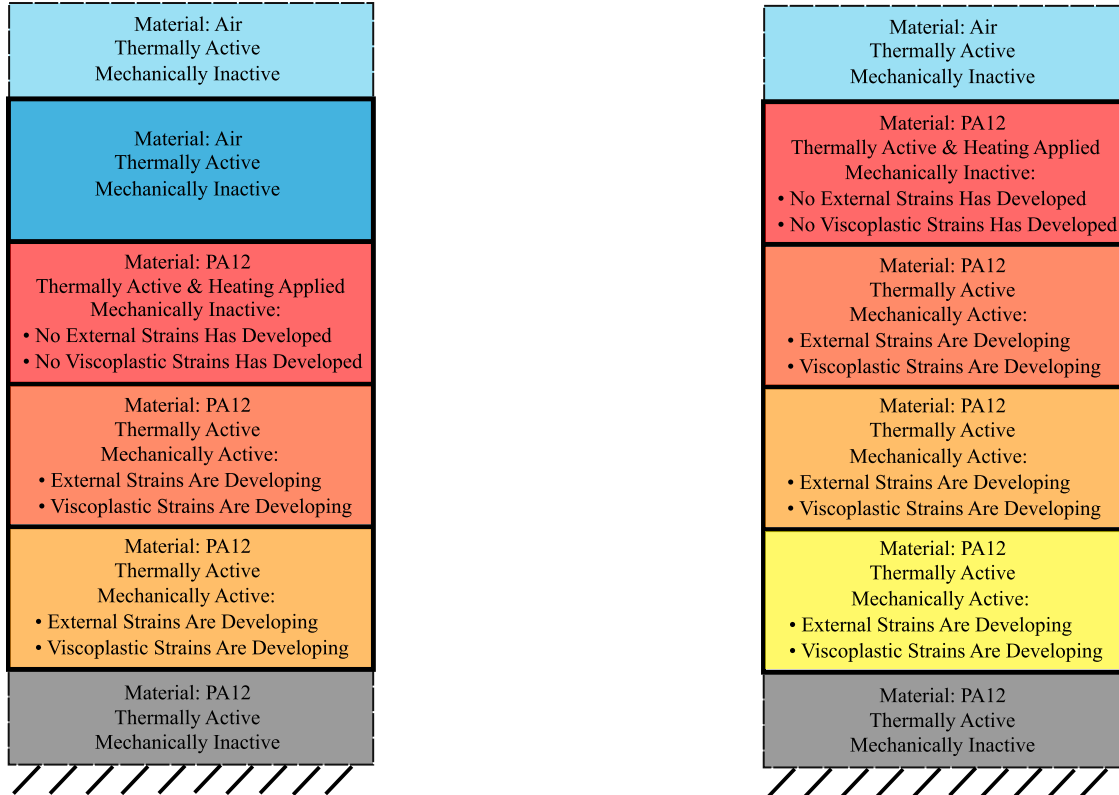
To sum up, a layer is only thought to be a single object once the sintering is done, meaning after the heating and the cooling in between layers is done. This is the reason why, for the first step in Fig. 19a the first layer remains mechanically inactive while it gets heated. As the next layer is heated, as shown in Fig. 19b, the previously sintered layer has become one solid object, and all indirect heating received by the first layer causes external, expanding strains. However, since no other layers have been sintered yet, nothing restricts the expansion of the first layer, meaning no elastic strains develop, leading to no stresses, and for that reason, the yield stress isn't exceeded, and no viscoplastic strains develop for the first layer at this stage. For the third step, shown in Fig. 19c, all indirect heat now affects two already sintered layers. As the second layer will receive more indirect heat, it will expand more than the first layer, leading to elastic strains. These elastic strains lead to von Mises stresses that trigger the viscoplasticity, and so for the first two layers, viscoplastic strains develop. Fig. 19d shows the last step, which is similar to the third step, except one additional layer is now mechanically active.

Lastly, in Fig. 19 the bottom layer and top layer, which act as "buffer" layers, need to be addressed. These buffer layers ensure that no layers are affected by any boundary effects, and as such, all exhibit the same behavior. The bottom layer is fixed at the bottom, and it consists of PA12 that is thermally active and mechanically inactive throughout the entire simulation. The top layer is thermally active and mechanically inactive air throughout the entire simulation. Also, any layer that is yet to be heated is also thermally active, mechanically inactive air.



(a) Heating of 1st layer.

(b) Heating of 2nd layer.



(c) Heating of 3rd layer.

(d) Heating of 4th layer.

Figure 19: Overview of thermal and mechanical activation of each layer.

3.3 MESHING AND TIME-STEPPING

For ease of meshing and to guarantee uniform element distribution across layers in the build direction, the identity mapping feature in COMSOL is applied during meshing. This essentially voxelizes the geometry, allowing the entire part to be embedded within a simple box-shaped build chamber. This chamber can then be easily discretized using quadrilateral elements.

Variations in mesh density were explored. These included different element sizes applied in the build plane and mesh resolutions of one to three elements per layer along the build axis.

A mesh with 3.2 mm element size in the build plane (zy-plane) of the beam is illustrated in Fig. 20.

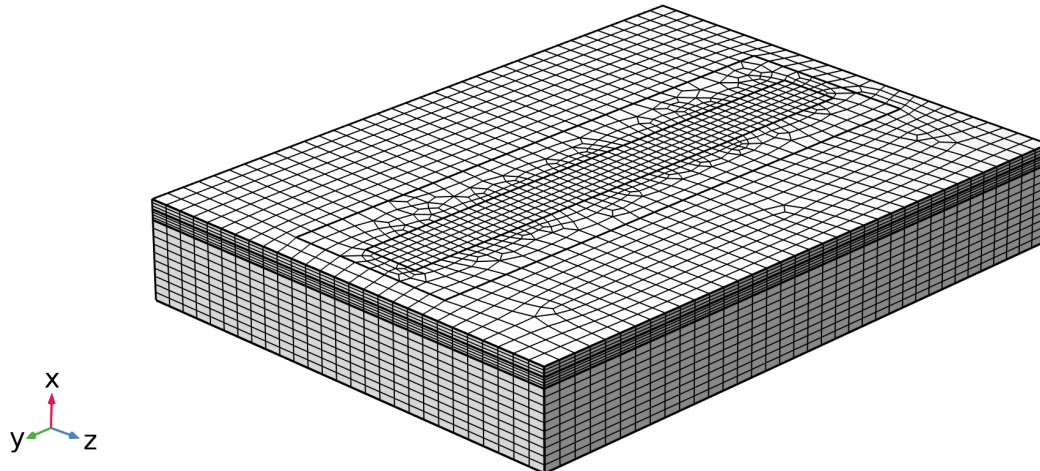


Figure 20: Full build-chamber geometry with beam at the center meshed with 3.2 mm element size. The beam is surrounded by loose powder at a coarser mesh size. The loose powder has a thickness of 24 mm below the beam and 4 mm above the beam.

Furthermore, to maintain numerical stability, the Courant number is employed [24].

$$C = V_x \cdot \frac{\Delta t}{\Delta x} \quad (23)$$

A Courant-Friedrichs-Lowy (CFL) condition of $C < 1$ is enforced to ensure that each time step is sufficiently small relative to the spatial discretization. From this, the maximum allowable time step is derived as follows:

$$\Delta t = \frac{L_x}{V_x \cdot N_{ele}} \quad (24)$$

Here, $\Delta x = L_x/N_{ele}$ defines the spatial resolution of the grid, where L_x is the length of the domain in the build direction and N_{ele} the number of elements across that length.

3.3.1 Element Discretization Type

When meshing a geometry, it is important to consider the element order with which you are meshing. The order describes the polynomial degree of the shape functions used within the element to approximate the solution. As such, first-order elements, also called linear elements, use shape functions of polynomial degree 1, they have 2 nodes and use linear interpolation in between nodes, as shown in Fig. 21a. Second-order elements, also called quadratic elements, use shape functions of polynomial degree 2, they have 3 nodes (2 endpoints and 1 midpoint) and use parabolic interpolation in between nodes, as shown in Fig. 21b [2].

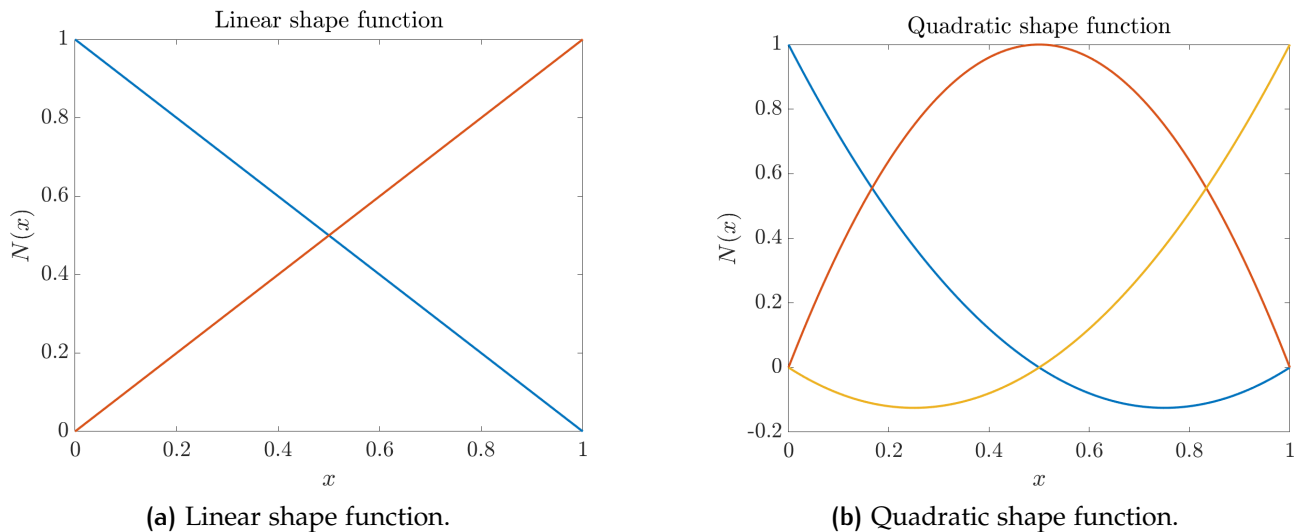


Figure 21: Comparison of linear and quadratic shape functions [2].

Additionally, using quadratic shape functions also helps capture curved geometry better, as depicted in Fig. 22.

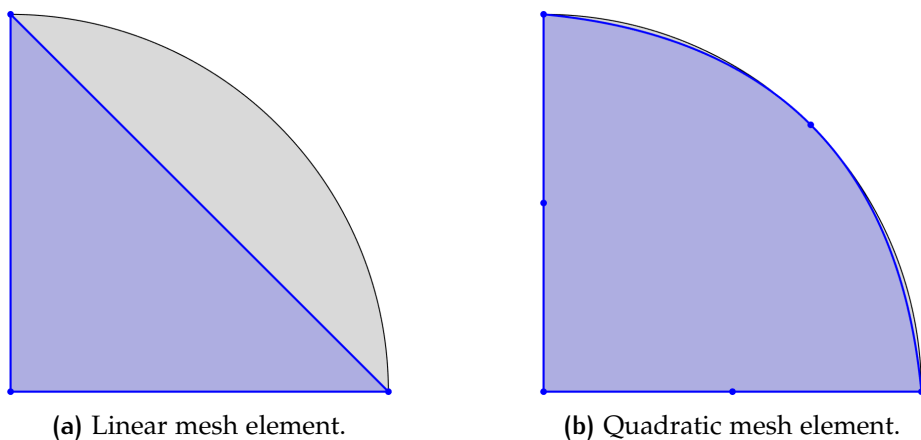


Figure 22: Comparison of linear and quadratic mesh elements [2].

Because of their extra node and curved interpolation, quadratic elements can better approximate smooth gradients and curved physical behavior within a single element. This means that [2]:

- Quadratic elements can achieve a given level of accuracy using fewer elements than linear elements.
 - Despite having more degrees of freedom per element, the total number of elements and global degrees of freedom may be lower, leading to reduced computational effort.
 - They are particularly effective in modelling problems with smooth gradients, such as beam bending, diffusion processes, or heat conduction in smoothly varying domains.

However, in regions with sharp gradients, quadratic interpolation may introduce overshooting or spurious oscillations. In such cases, mesh refinement using linear elements may yield more stable and physically accurate results. Therefore, the choice between mesh density and element order should be made based on the nature of the solution and the problem domain [25].

Thus the framework of the simulation is established. The following table lists the used parameters:

Parameter	Value
Hatch spacing, H	0.36 mm
Velocity in build direction, V_{scan}	1.1 m s ⁻¹
Max laser power, P_{max}	15.8 W
Absorptivity, ξ	0.4
Energy scale factor, E_{scale}	0.45
Print chamber z-length	150 mm
Print chamber y-length	200 mm
Flash heating exposure time, t_{heat}	0.0012 s
Bed temperature, T_{bed}	177.5 °C
Powder temperature, T_0	175 °C
Surface emissivity, ϵ	0.8
Heat transfer coefficient at the sides of the build chamber, $h_{\text{tc},\text{sides}}$	10 W K ⁻¹ m ⁻²
Heat transfer coefficient with the air, h_{tc}	15 W K ⁻¹ m ⁻²
Thermal conductivity of solid PA12, k_{solid}	0.23 W K ⁻¹ m ⁻¹
Density of solid PA12, ρ_{solid}	1030 kg m ⁻³
Poisson's ratio, ν	0.4
Viscoplastic parameter, λ_0	0.0015 s ⁻¹
Viscoplastic parameter, γ	0.9
Viscoplastic parameter, p_y	0.03
Viscoplastic parameter, m	5
Latent heat of fusion, LH	145 J g ⁻¹
Specific heat capacity outside sintering region, $Cp0$	2 J g ⁻¹ K ⁻¹
Solidification temperature, T_s	155.3 °C
Melting temperature, T_m	186.2 °C
Crystallization temperature, T_c	150 °C

Table 1: Parameters used for the flash heating model

3.4 EXPERIMENTS

3.4.1 Printing of Specimens

The printing is performed on the Sinterit Lisa X printer, as seen in Fig. 23:



Figure 23: The Lisa X Printer.

In the associated slicer software, Sinterit Studio, a shrinkage scaling factor is specified. What this means is that the printer overdimensions the part by just enough such that the final dimensions match the uploaded file for the part. However, this shrinkage scaling factor can only be slightly adjusted and cannot be completely turned off — which would have been desirable for the purposes of this work to be able to compare total shrinkage with the simulations. In the Sinterit Studio software, it can also be checked that the temperature of the powder bed and the temperature in the chamber match the values in the simulation. Once the printing is done and the powder cake is received, the amount of powder on either side of the part and the powder left at the bottom of the print chamber can be measured, and these values used in the simulation. For the beams, a powder thickness of 24 mm underneath the part and 4 mm above the part has been measured.

3.4.2 Cooling Experiment

For the simulations, it is necessary to know the temperature within the build chamber during the cooling phase. The temperature was logged during this phase, and the recorded data is shown in Fig. 24. Additionally, a function has been fitted to the data, enabling extrapolation beyond the bounds of the measured values.

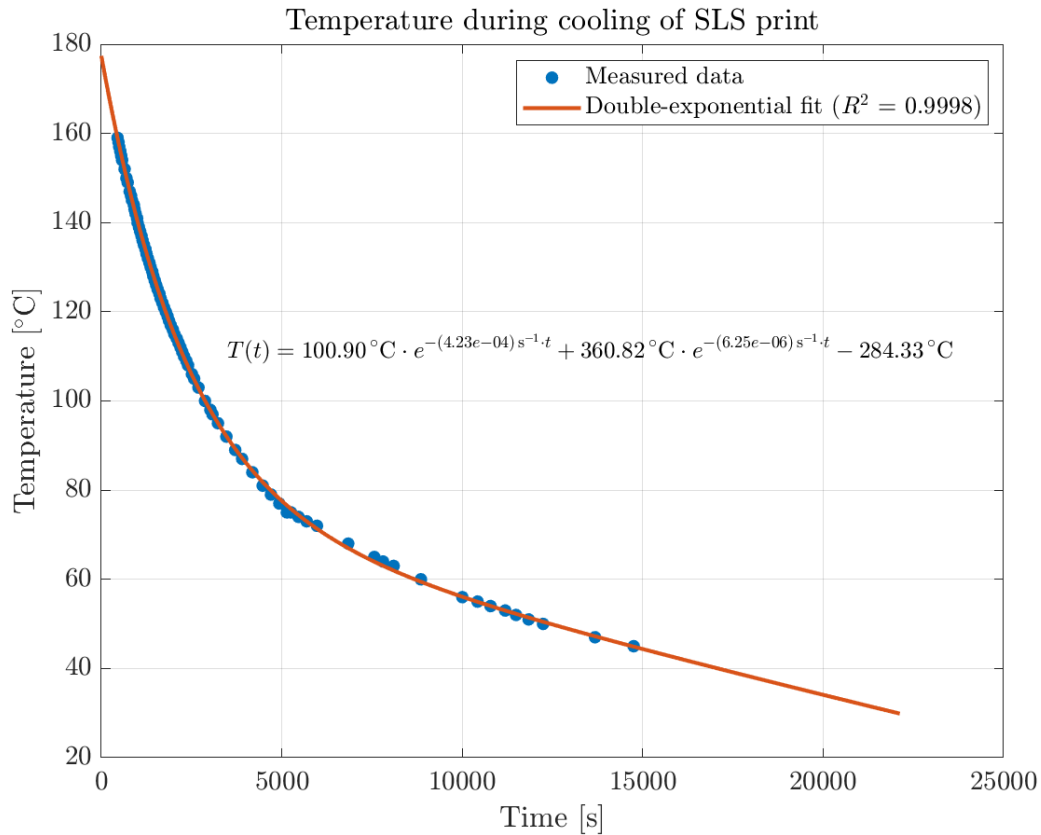


Figure 24: Experimentally found temperature in the build chamber during the cooling phase.

3.4.3 Measurements

After printing, the warpage needs to be measured. This is done using the 3D-scanner function of the Keyence VR-3200 Macroscope, which at high magnification has a tolerance of $\pm 2 \mu\text{m}$ [26]. The microscope can be seen in Fig. 25.



Figure 25: The Keyence VR-3200 macroscope.

By measuring the distance from one face, through-thickness, and down to the bed of the macroscope, and then flipping the beam 180 degrees lengthwise and measuring the same through-thickness value from the other side, the difference between these two measurements gives a value for the warpage.

3.4.4 Bridge Curvature Method

In this work the warpage of a bridge-shaped part will be investigated as well. The reason the bridge shape is used is that it has two large masses on either side that cool down slower than the edges. This mismatch in cooling rate can introduce warpage. This shape is commonly used, especially for metal parts printed using selective laser melting (SLM), to measure warpage, as the bridge tends to "open up," and the angle, as depicted in Fig. 26, can be used as a measure of warpage [27].

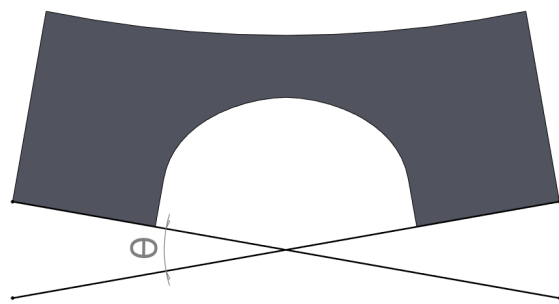


Figure 26: Illustration of the angle measured in the bridge curvature method.

In SLM, the bridge is bonded to the print bed, which aids in the buildup of residual stresses that lead to warpage once the part is separated from the bed, and since the part is not bonded to the print bed in SLS, the viability of using the bridge curvature method in SLS will be assessed [12].

RESULTS AND DISCUSSION

4.1 SIMULATION RESULTS

To assess the accuracy and reliability of the simulation, both thermal and mechanical results are monitored and analyzed. The thermal response is particularly critical in powder bed fusion processes, as it directly influences the thermal and mechanical properties of the final part. The simulated thermal data is therefore monitored in detail across the different stages of the build process to ensure consistent behavior and to identify potential discrepancies or artifacts.

The initial focus is placed on understanding the temperature distribution and its direct effect on density. Fig. 27 depicts a section view of the temperature at the end of the heating phase, and Fig. 28 depicts the corresponding density.

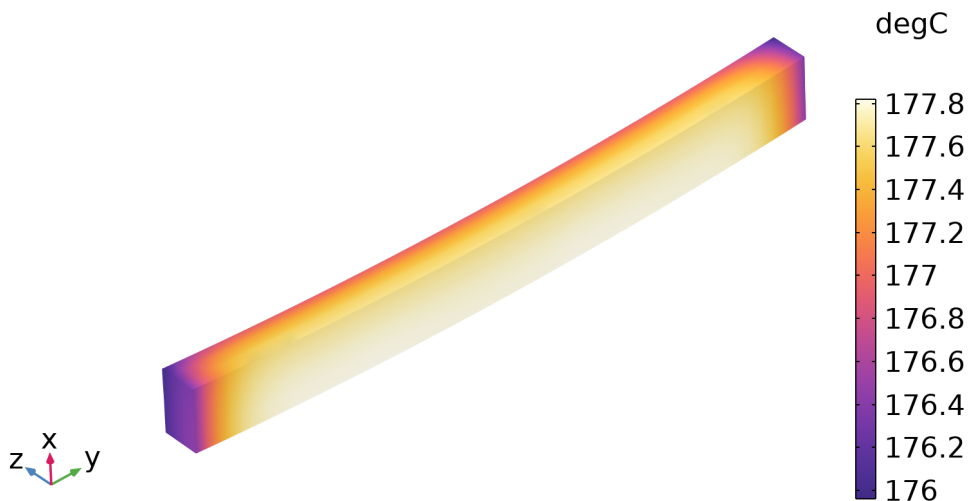


Figure 27: Temperature at the end of the heating phase sectioned in the xy -plane. The color legend represents temperature values, while the deformation of the geometry is visually included in the plot. Note that the x -axis has been stretched by a factor of 5 for visualization purposes, meaning the apparent deformation is also visually exaggerated by this factor.

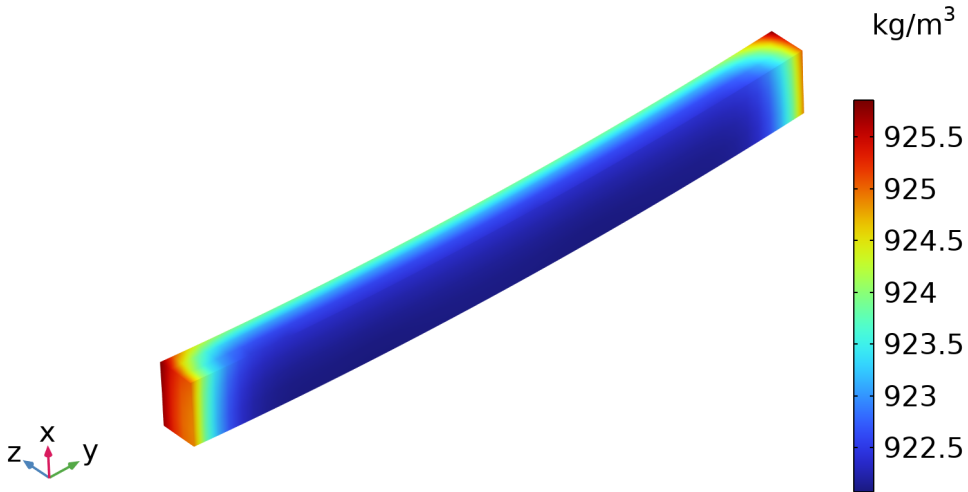


Figure 28: Density at the end of the heating phase sectioned in the xy -direction. The color legend represents values of density, while the deformation of the geometry is visually included in the plot. Note that the x -axis has been stretched by a factor of 5 for visualization purposes, meaning the apparent deformation is also visually exaggerated by this factor.

While Figs. 27 and 28 provide valuable insight into the relationship between the spatial distributions of temperature and density at a fixed point in time, they do not capture the dynamic nature of the thermal process throughout the build. To fully understand the thermal history and how heat is transferred and retained within the part over time, it is essential to analyze the temporal evolution of temperature at key locations.

Fig. 29 illustrates this by showing the temperature over time at the center of each layer in a 4-layer beam. This temporal perspective reveals the characteristic heating and cooling behavior associated with the layer-by-layer nature of the SLS process.

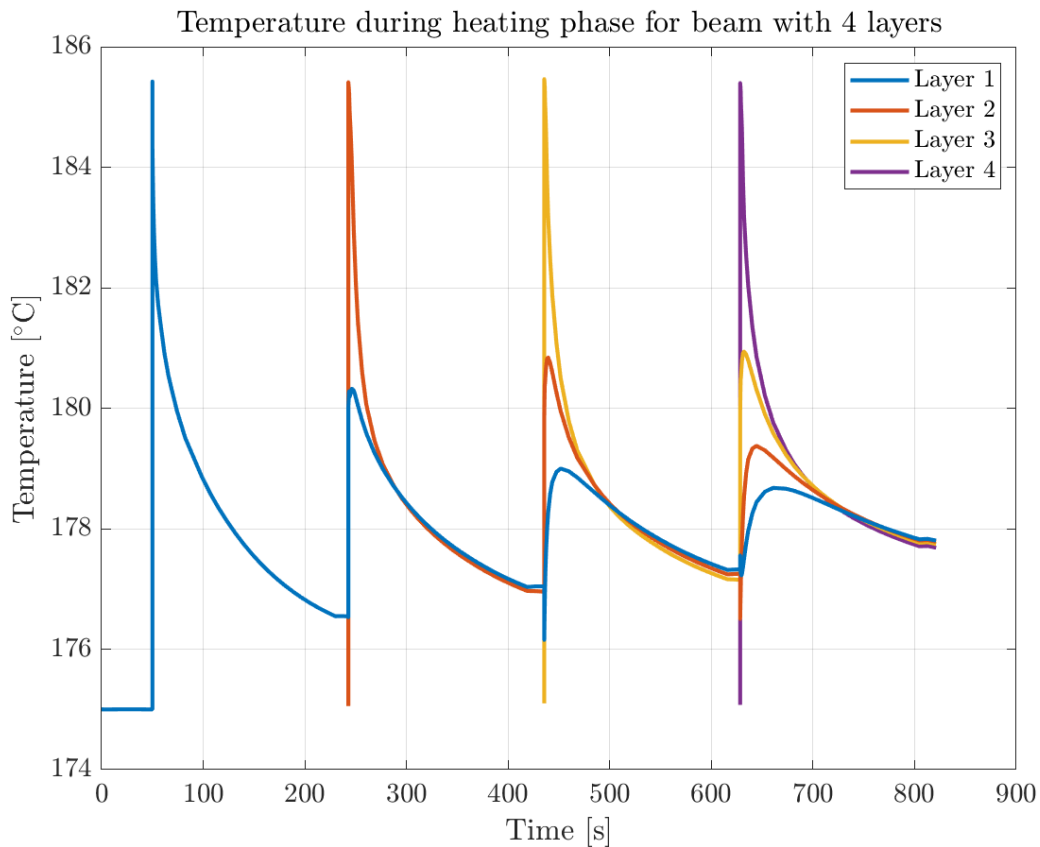


Figure 29: Temperature in the heating phase at the center of each layer of a 4 layer beam.

As each layer is activated, the temperature rises sharply up to about the melting temperature of PA12. Afterwards the temperature gradually decreases. As subsequent layers get heated, some residual heat causes the temperature of previous layers to rise by an amount that is dependent on the distance between any two layers. The first layer is heated at $t = 50$ s, and in Fig. 29 all subsequent layers are only depicted from the point at which they get activated and onward. However, in reality the subsequent layers consist of air before they get activated, and as such they do increase in temperature before activation. In Fig. 30 the temperature for layer 2 both before and after activation is depicted.

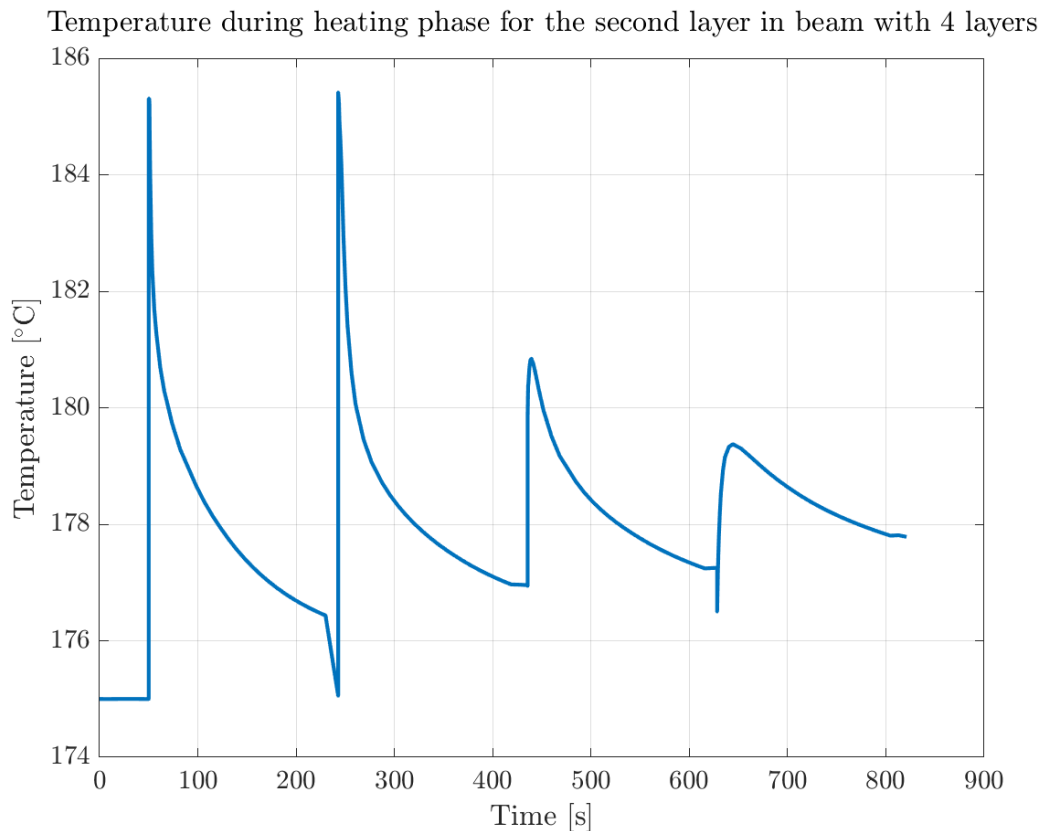


Figure 30: Temperature in the heating phase in the 2nd layer of a 4 layer beam.

As seen in Fig. 30 as the first layer is activated at $t = 50\text{ s}$, the second layer receives a lot of heat. This, however, makes it necessary to "reset" the temperature before it is activated, as when the second layer goes from being air to powder, the powder needs to start at temperature $T_0 = 175\text{ }^\circ\text{C}$ as described in section 3.2. This reset happens at $t = 236\text{ s}$ in Fig. 30.

Fig. 31 is created to illustrate the temporal evolution of the density during the heating phase, which shows the density corresponding to the temperatures depicted in Fig. 29.

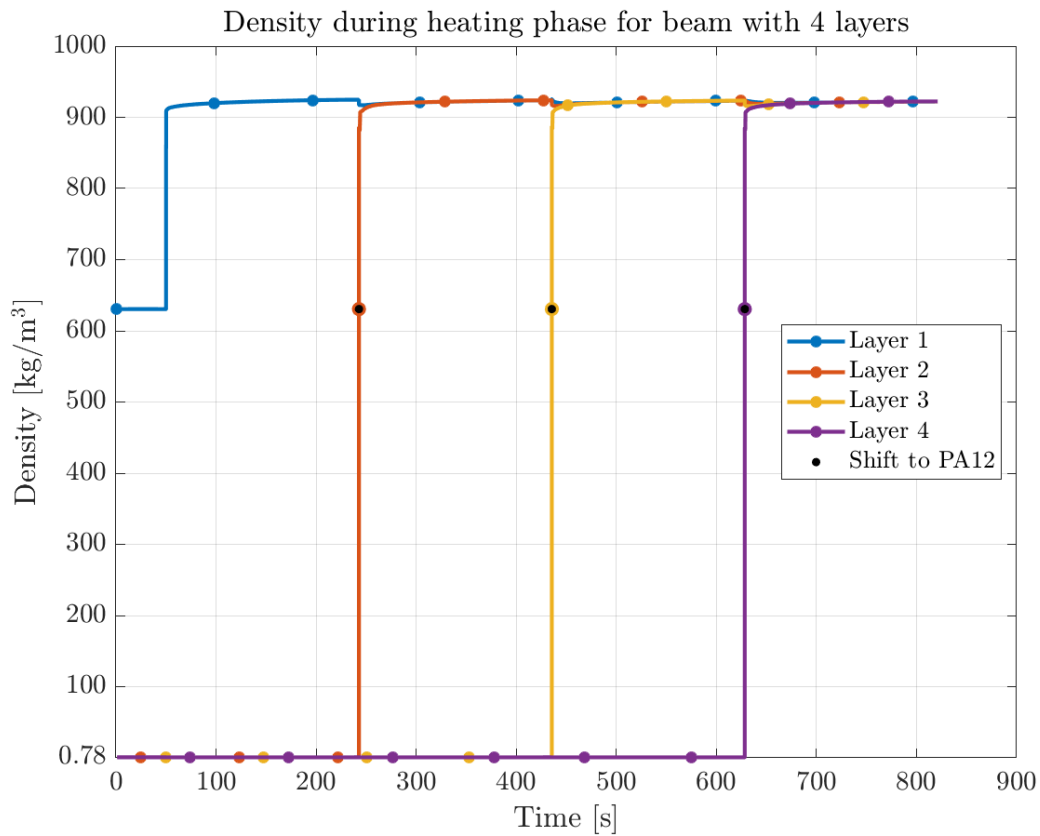


Figure 31: Density for each layer for 4 layer beam. Note that the point of transition from air to PA12 is marked in black for layers 2-4.

The first layer starts as unsintered powder at a density of 630.56 kg m^{-3} , and the other layers are air with a density of 0.78 kg m^{-3} up until activation. The point where the layers transition from air to PA12 is marked with a black dot in Fig. 31.

While Figs. 29 - 31 focus on the heating phase and highlight the thermal interactions between adjacent layers during activation, they do not capture the longer-term thermal evolution once the energy input ceases. To fully understand the thermal behavior, it is important to also examine the cooling phase, during which further solidification occurs.

Fig. 32 presents the complete thermal history for the 4-layer beam, including both the heating and cooling phases.

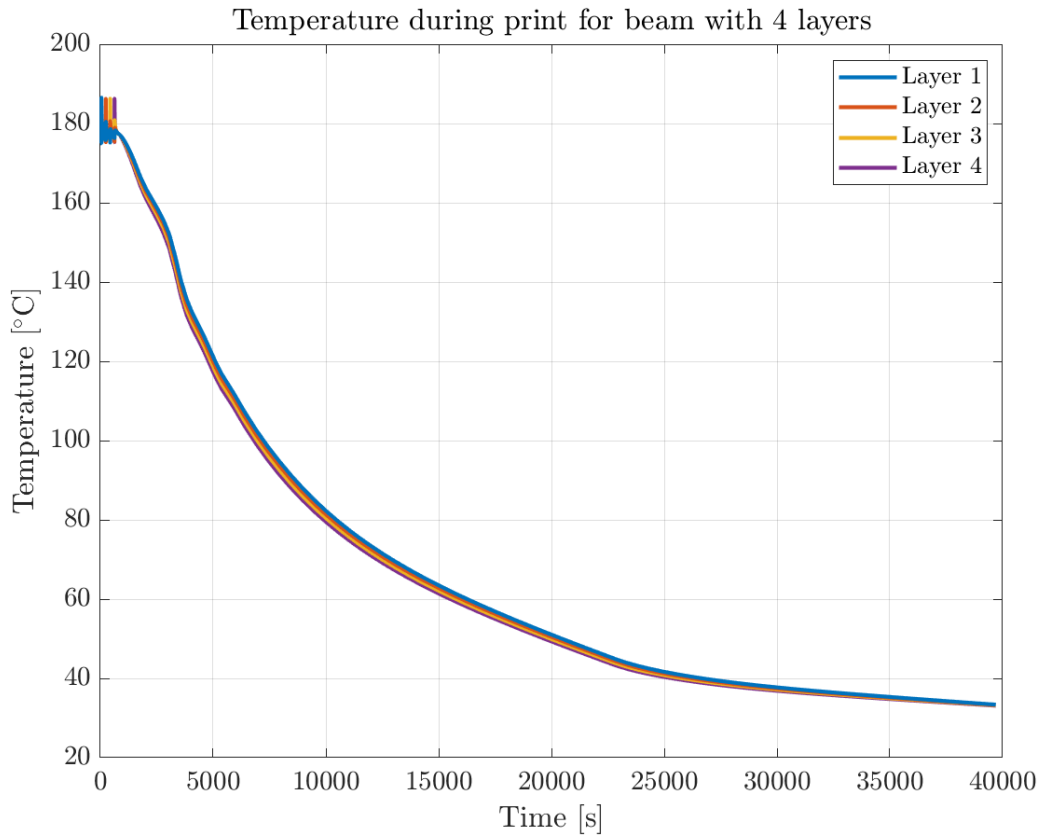


Figure 32: Temperature during heating and cooling phase for beam with 4 layers.

This figure reveals that the upper layers initially cool more rapidly than those below, due to their more immediate exposure to ambient conditions. Additionally, in the simulation setup, the beam is embedded within a powder bed consisting of some unsintered powder beneath it and some unsintered powder above it. To avoid warpage the Lisa X printer allows for removal of the parts once the temperature drops below 50 °C [4], but in the case of the experiments the parts were allowed to cool down to ambient temperature.

While the cooling behavior offers valuable insights into the thermal history of the printed part, the mechanical consequences of the thermal cycles are equally critical to understanding the warpage. These stresses can exceed the temperature-dependent yield strength of the material, even if only momentarily, leading to localized viscoplastic deformation. This mechanical behavior is examined in detail in the following section, beginning with an analysis of von Mises stress evolution during the activation of the 1st layer, Fig. 34.

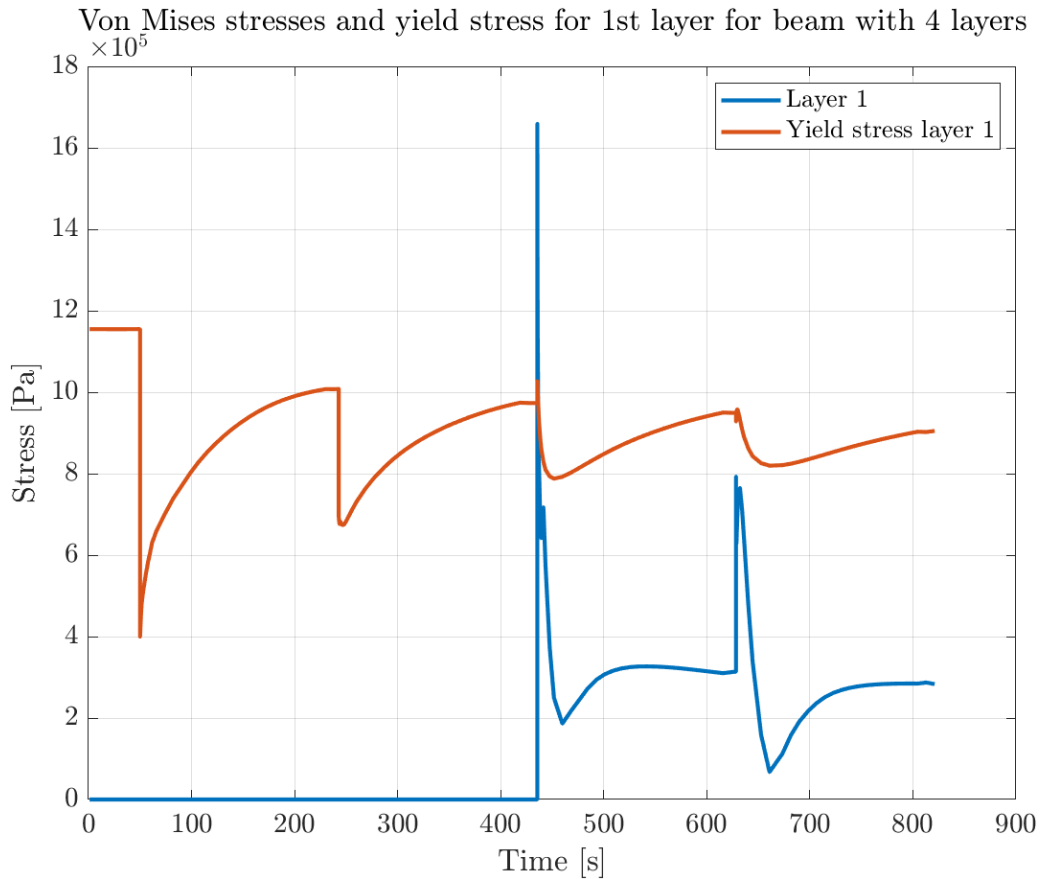


Figure 33: Stresses in the 1st layer pf beam with 4 layers, along with the yield stress.

Fig. 33 shows the temperature-dependent yield stress of the 1st layer and how it briefly exceeds the yield stress at the point where the 3rd layer gets activated. Fig. 34 further illustrates the stress evolution at the center of each layer.

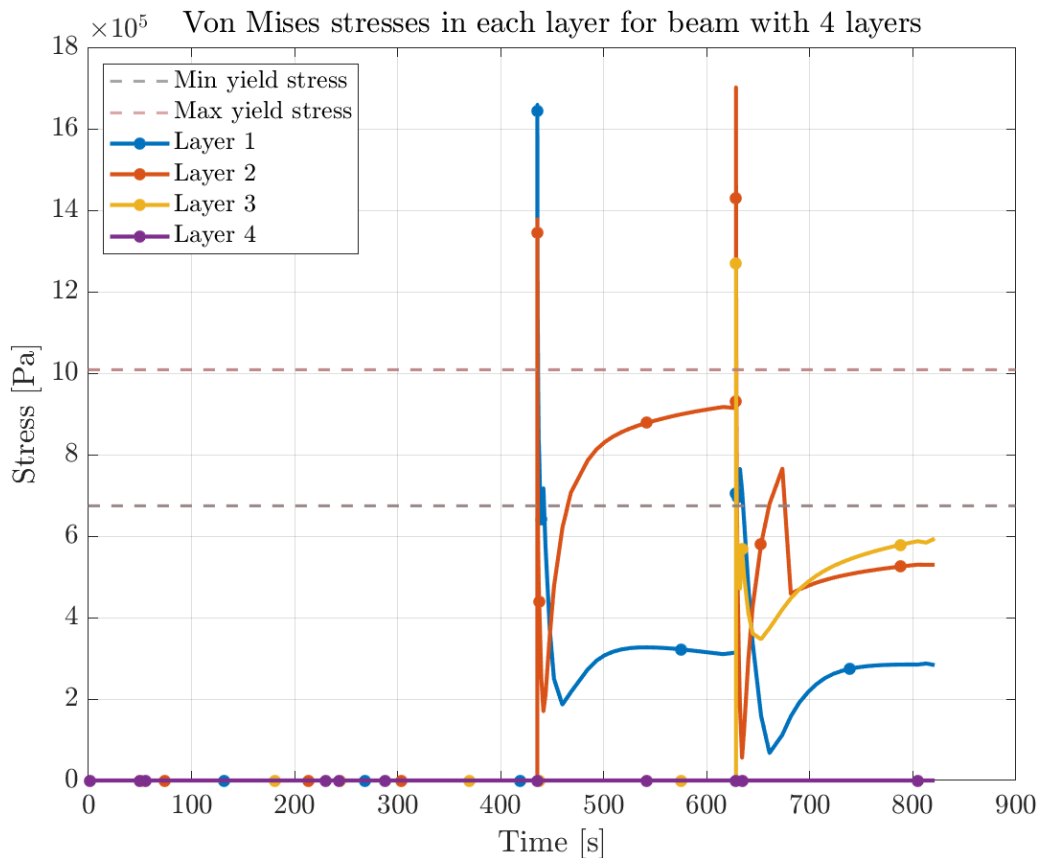


Figure 34: Stresses in beam with 4 layers, along with the maximum and minimum yield stress reached during printing.

As the temperature is different in each layer, the yield stress is different, so the maximum (at $\sim T = 176.5^\circ\text{C}$) and minimum (at $\sim T = 181^\circ\text{C}$) yield stress are plotted as a general guideline, thus it is possible to get an idea when every layer exceeds and drops below the yield stress. In Fig. 34 it is observed that the spikes in von Mises stresses happen in pairs, meaning when layer 3 is activated, both layer 1 and layer 2 exceed the yield stress. Layer 2 then exceeds the yield stress once more, alongside layer 3, when layer 4 is activated.

This behavior translates directly to the onset of viscoplasticity, as shown in Fig. 35.

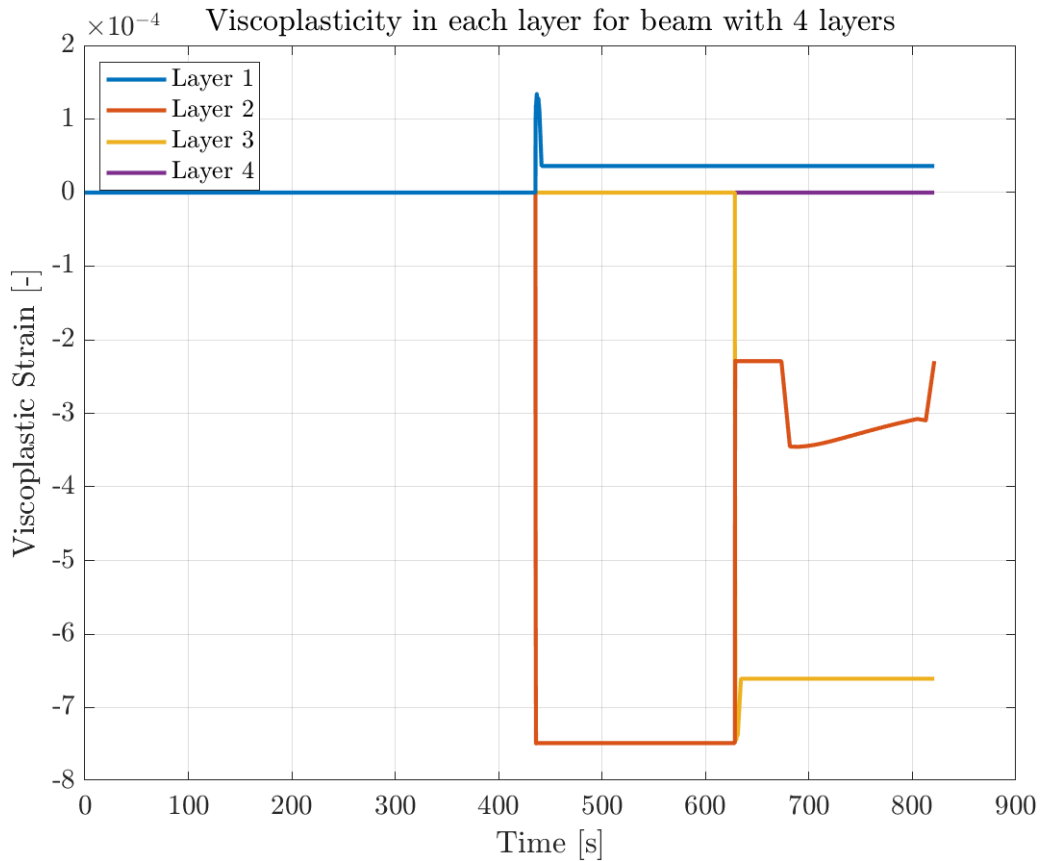


Figure 35: Viscoplastic strains in beam with 4 layers.

Note that the final layer doesn't have any viscoplastic strains as described in Fig. 19. For the other layers, the viscoplastic strains get more and more negative for subsequent layers, this is one of the main effects causing warpage during the heating phase.

For the first mechanical activation, the interaction between layer 1 and layer 2 causes positive viscoplastic strains to occur in the first layer and negative viscoplastic strains to occur in the second layer. This is because as the second layer expands the first layer is put in tension and the second layer in compression. As the third layer is activated at around $t = 628\text{ s}$ a similar interaction happens between the second and the third layer, which causes the viscoplastic strains in the second layer to increase, however the viscoplastic strains remain negative. Additionally, at the point of the third activation at $t = 628\text{ s}$ the viscoplastic strains of the first layer don't change as the stresses don't increase enough for the yield stress to be exceeded.

Further investigating the mechanical response, in this instance for the 2nd layer, yields the temporal evolution of the three different strain components depicted in Fig. 36.

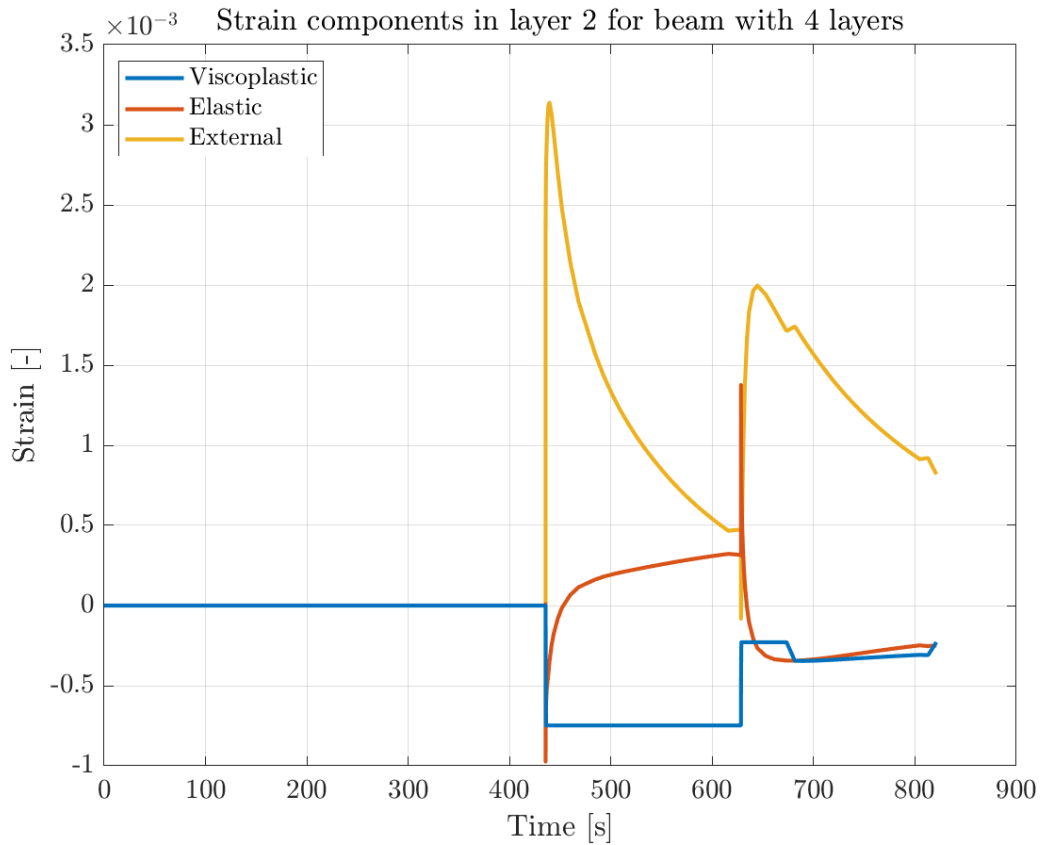


Figure 36: Strain components in beam with 4 layers for layer 2.

It is observed that as the temperature increases, the density decreases, leading to thermal expansion, which can be seen as the positive external strains in Fig. 36. As the layer beneath (1st layer) doesn't receive as much heat, it doesn't expand as much as the 2nd layer. For this reason the 2nd layer is partially restricted by the 1st layer and thus not free to expand. Therefore, negative elastic strains develop in the 2nd layer, and once these negative elastic strains lead to von Mises stresses that exceed the yield stress, negative viscoplastic strains occur.

4.1.1 Numerical Analysis

Ensuring numerical convergence is essential for the reliability of any simulation. Convergence studies typically involve assessing the sensitivity of the results to various numerical parameters, among which the relative tolerance is particularly significant. Fig. 37 illustrates the influence of the relative tolerance — a common solver parameter that governs the acceptable error in relation to the magnitude of the solution — on the computed warpage. What Fig. 37 depicts is that the relative tolerance must be set to a low enough value such that the solution doesn't change substantially if the relative tolerance were to be decreased

further. For the simulation used in Fig. 37, which has 3.2 mm mesh size, linear elements, 1 element per layer, and 4 layers total, it is found that a relative tolerance of 0.01 is sufficiently low in the sense that decreasing the relative tolerance further doesn't change the result more than 5%.

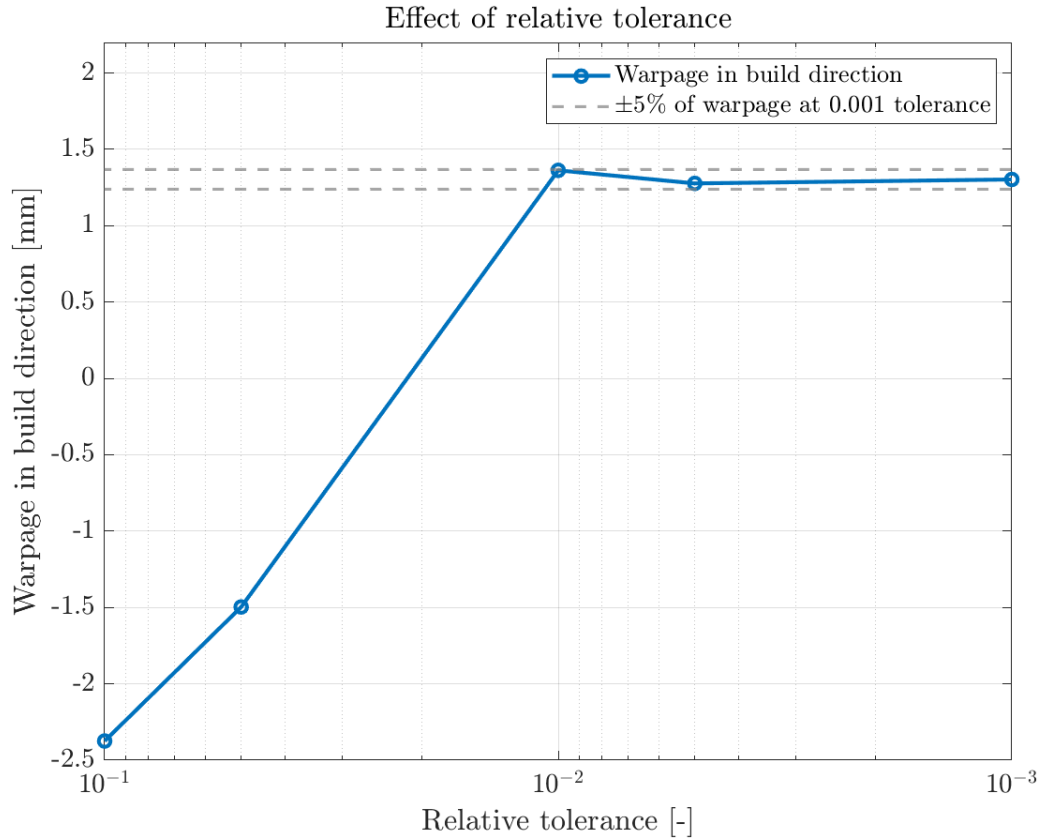


Figure 37: Warpage as a function of relative tolerance for: 3.2 mm mesh size, linear elements, 1 element per layer, 4 layers total.

The relative tolerance must be ensured to be low enough for all simulations, and for that reason, for the following results, a relative tolerance of at least 0.001 has been used.

Two other parameters of importance are the in-plane mesh element size and the element discretization type, as described in section 3.3.1. In Fig. 38 it is depicted how the quadratic serendipity element type struggles to converge with decreasing element size to a value within 5%.

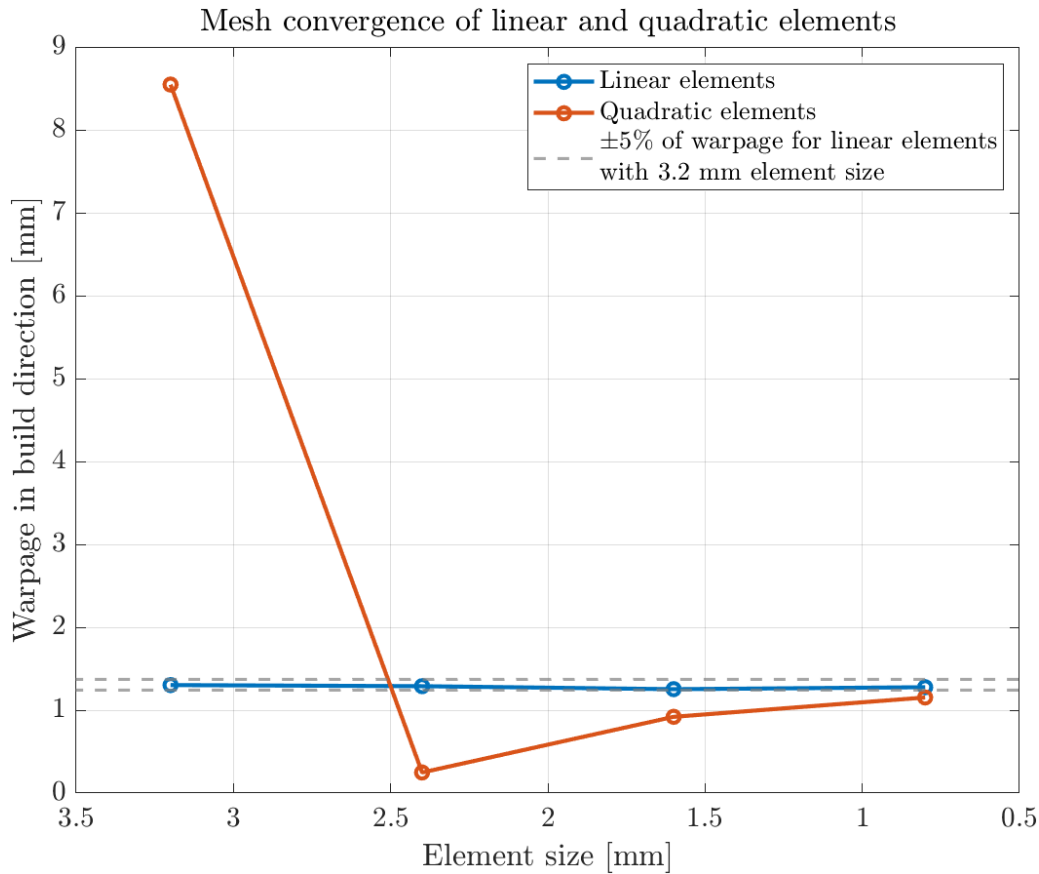


Figure 38: Effect of element type for: relative tolerance 0.001, 1 element per layer, 4 layers total.

In the linear case only the heat transfer problem has been meshed with linear elements, the solid mechanics is meshed with quadratic elements. In Fig. 38 it can be seen that the case with linear elements converges much more easily compared to the case where only quadratic elements are used. The reason the quadratic elements struggle to converge might be due to a phenomenon termed "spurious oscillations due to small time increments," in which inaccurate solutions can occur for quadratic elements in cases with temperature-dependent material properties if the temperature changes rapidly at too small time increments [25].

Additionally, for all simulations, it is important to ensure that the mesh size is sufficiently small such that the simulation is converged. For the case depicted in Fig. 38, where the relative tolerance is 0.001, there is 1 element per layer and 4 layers in total a mesh size of 3.2 mm is found to be sufficient for the linear case.

In addition to the in-plane mesh element size, it is also important to assess the discretization along the build direction. The influence of increasing the number of elements in the build direction is illustrated in Fig. 39.

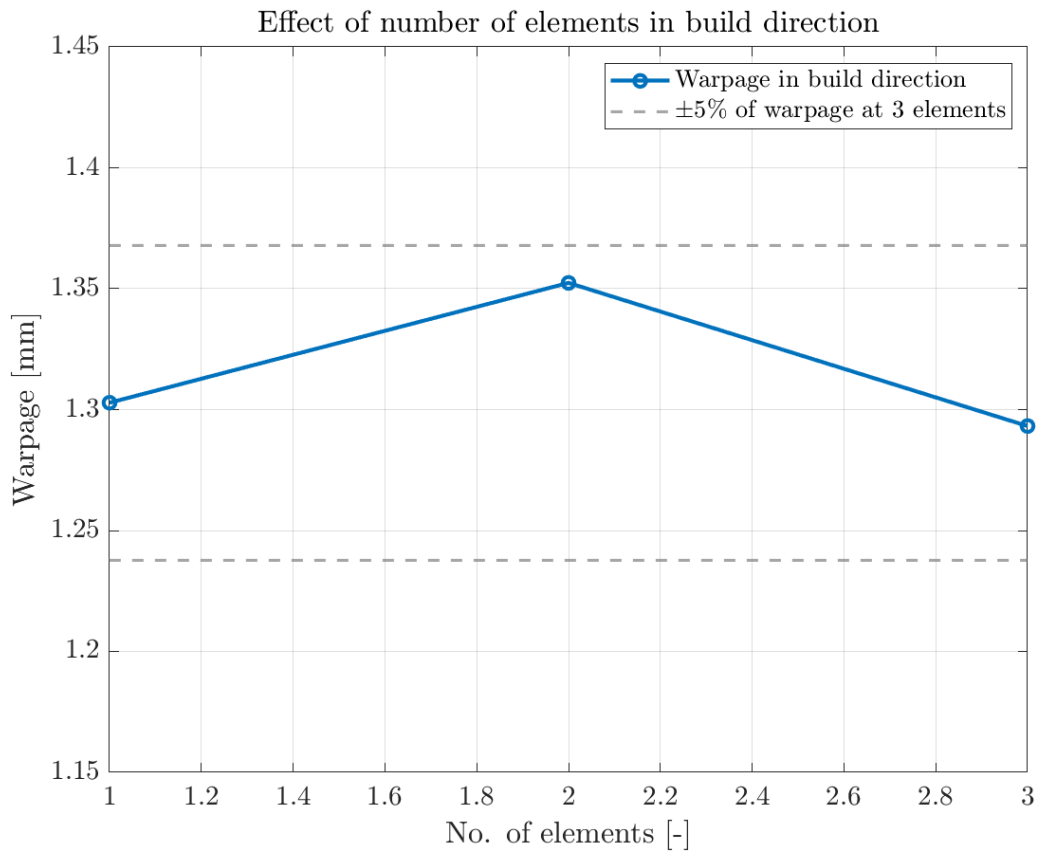


Figure 39: Effect of number of elements in build direction for: relative tolerance 0.001, 3.2 mm mesh size, linear elements, 4 layers total.

As shown, increasing the number of elements from 1 to 3 per layer results in only marginal changes, indicating that a single element per layer is generally adequate for capturing the thermal and mechanical responses under the given conditions.

Beyond element resolution within layers, the number of layers itself is another parameter of interest. This is depicted in Fig. 40. For all the simulations with different numbers of layers, it was found that a relative tolerance of 0.001 is sufficient, but using the same mesh size as for the 4-layer simulation of 3.2 mm doesn't ensure mesh convergence for simulations with other layers. In general, a rule of thumb is that doubling the number of layers should be followed by halving the mesh size. This leads to a rapid increase in computational time with the number of layers, as with more layers not only must more heating events be resolved, but more elements are needed.

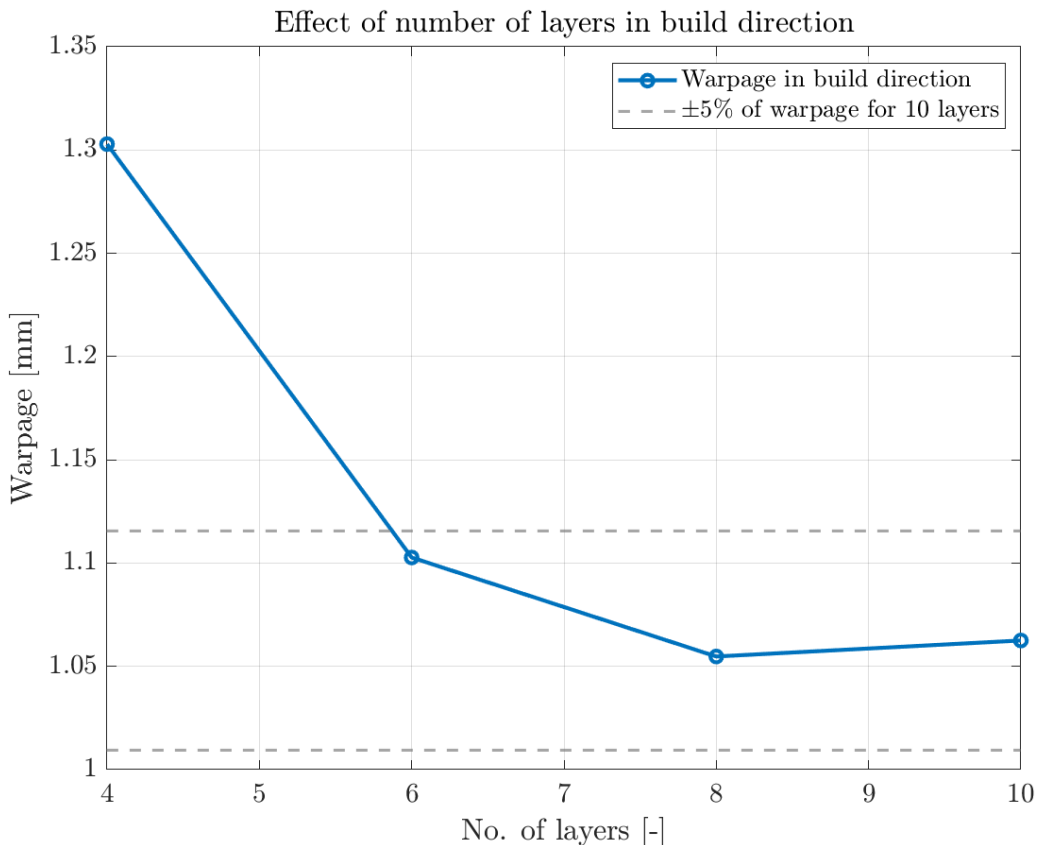


Figure 40: Effect of number of layers for: relative tolerance 0.001, appropriate mesh size, linear elements, 1 element per layer.

Fig. 40 shows that it is important to ensure that the number of layers is sufficiently high, and while it wasn't possible to investigate more layers due to lack of computational power, the results suggest that 6 layers are sufficient for the beam structure. 6 lumped layers correspond to flash heating ~5 layers at once, assuming a powder layer height between 0.1 mm and 0.125 mm. While 6 layers might be sufficient for the following results an 8-layer beam is used for additional fidelity.

4.1.2 Converged Results

Based on the results from section 4.1.1, an 8-layer simulation, with 1.6 mm in-plane mesh size, 1 mesh element in the build direction, and relative tolerance of 0.001, has been performed. Fig. 41 depicts the temperature distribution at the center of each layer.

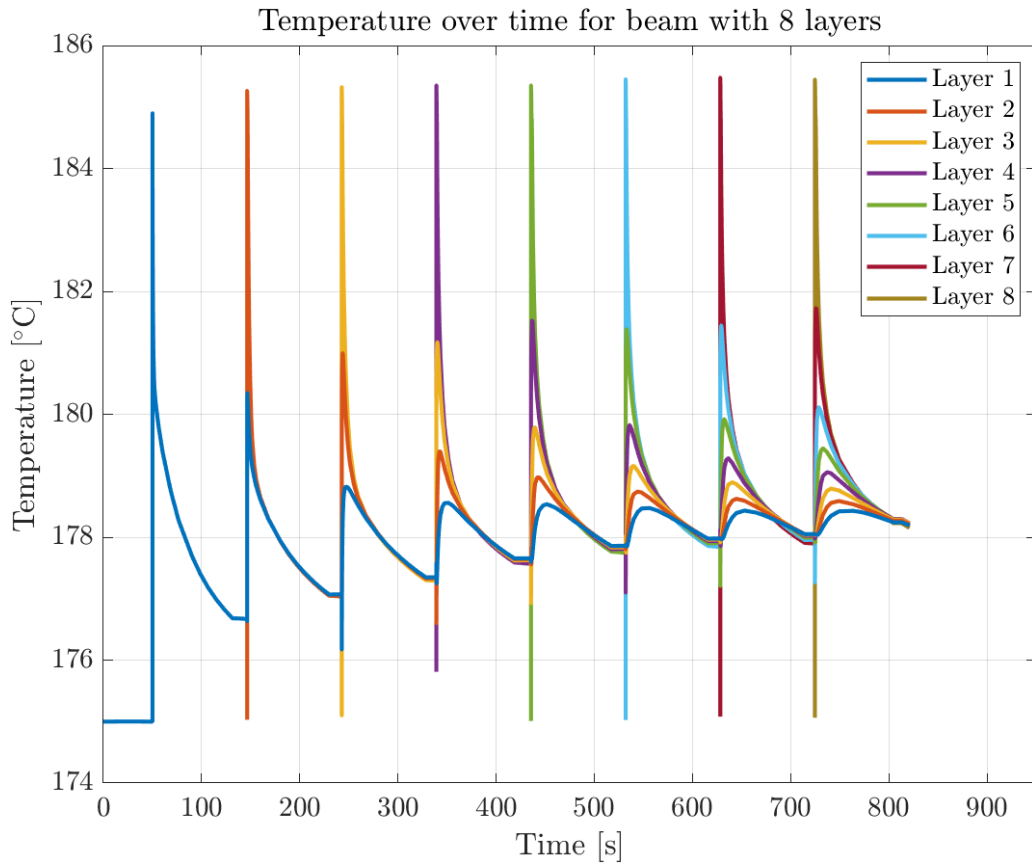


Figure 41: Temperature at the center of each layer in beam with 8 layers.

The main difference to note between Fig. 29 and Fig. 41 is that in Fig. 41 each layer has less time to cool down in between activations. After the heating phase, the position in the x -direction is shown in Fig. 42.

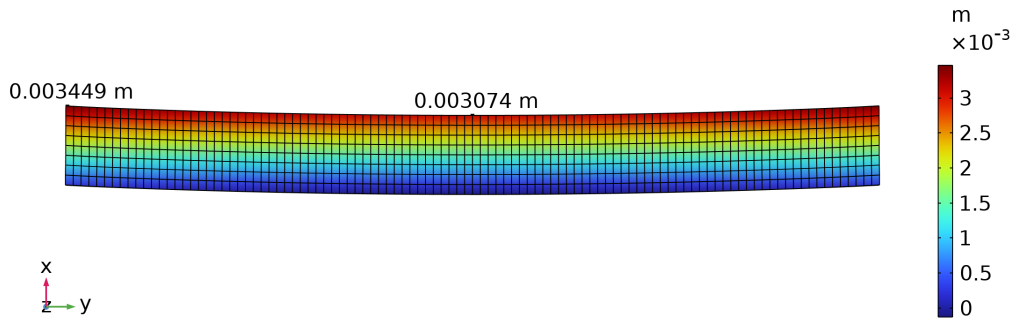


Figure 42: Position in build direction (x) at the end of the heating phase, for beam consisting of 8 layers. Position at the edge and the middle used to compute warpage is indicated on the figure. Note that the x -axis has been stretched by a factor of 5 for visualization purposes.

Thus, following the heating phase, the beam exhibits a warpage of 0.375 mm, as shown in Fig. 42. While this initial deformation is significant, it represents only a portion of the total warpage experienced by the part. The cooling phase introduces further warpage due to non-uniform temperature gradients across the beam. In particular, the top layers,

exposed to ambient conditions, cool more rapidly than the lower layers, resulting in a density gradient that drives additional warpage, as described in section 2.3. The density at the end of the cooling phase is illustrated in Fig. 43.

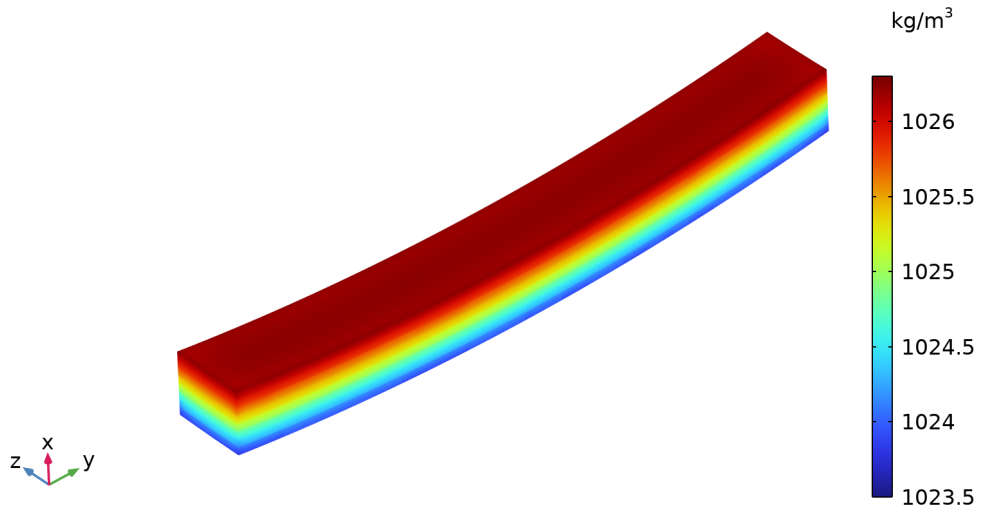


Figure 43: Density at the end of cooling of 8 layer beam. Note that the x -axis has been stretched by a factor of 5 for visualization purposes.

This leads to the strains and corresponding warpage illustrated in Figs. 44 and 45.

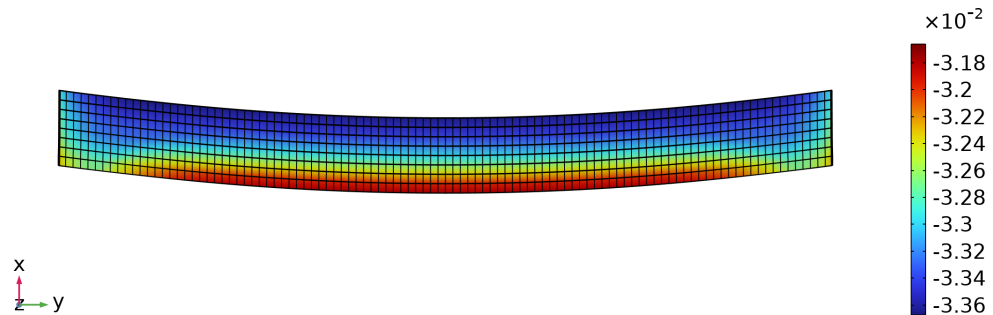


Figure 44: Strains in yy-direction at the end of the cooling phase, for 8 layer beam. Note that the x -axis has been stretched by a factor of 5 for visualization purposes.

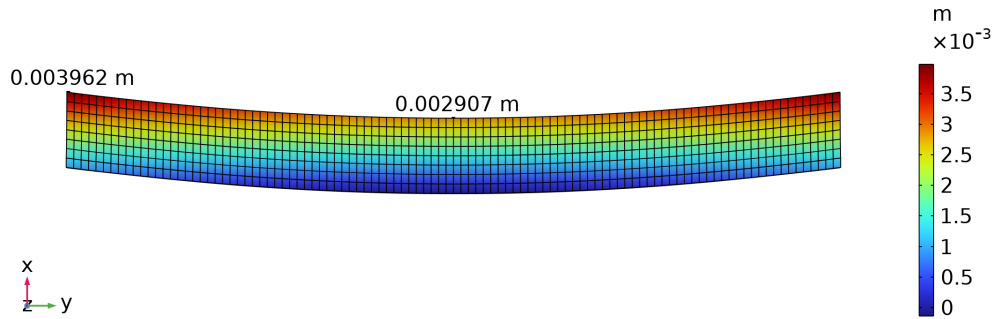


Figure 45: Position in build direction at the end of the cooling phase, for 8 layers. Note that the x -axis has been stretched by a factor of 5 for visualization purposes.

In total it warps by 1.055 mm. Comparing the warpage after the heating phase (0.375 mm) and after the cooling phase, it is quite common through all the performed simulations that the warpage after the heating phase is about 1/3 of the warpage after the cooling phase.

4.1.3 Experimental Results

When SLS-printing, the print comes out embedded within a "cake" of powder. The parts need to be properly removed from this cake in post-processing. The parts after removal from the cake appear as shown in Fig. 46.



Figure 46: Beam after removal of the cake.

After the careful removal of powder during post-processing, the beams are prepared for dimensional analysis to assess their deformation. To quantify warpage, each beam is

measured on both sides along specific directions termed the "bend"-direction and the "thickness"-direction. The bend-direction is shown in the macroscope in Fig. 47, where the slight bend can be seen between the beam and the base.

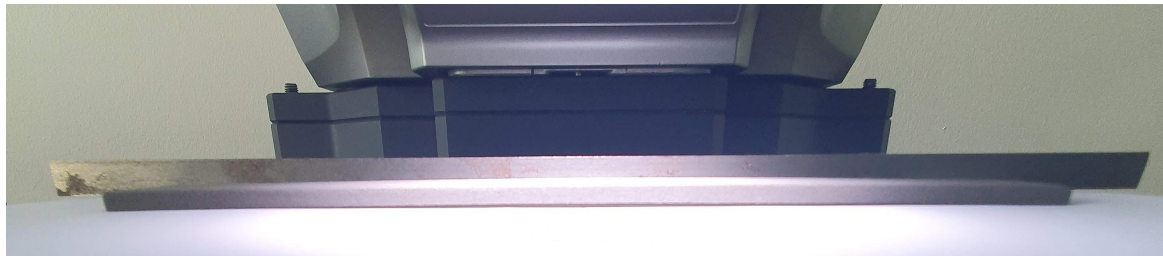
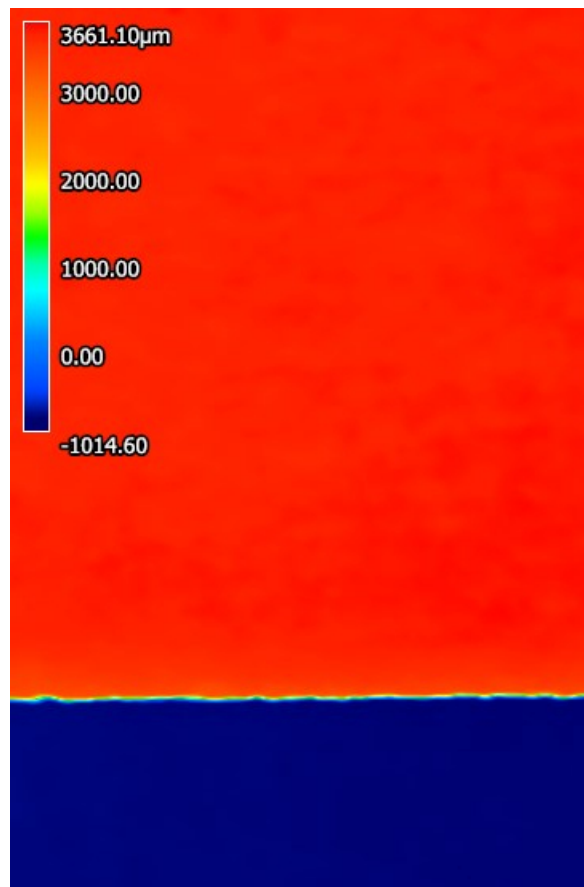


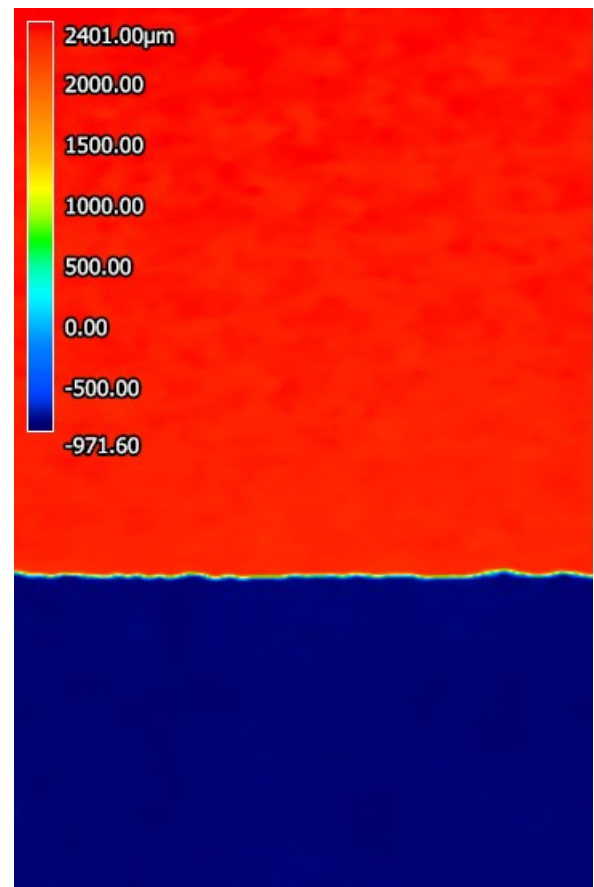
Figure 47: Measuring the bend-direction of a beam in the macroscope.

For the thickness-direction the beam is rotated 180 degrees lengthwise and the thickness measured on the same side.

In total, 4 beams have been printed. The following shows how the images of measurement look for the first beam.



(a) Beam 1 – Bend View.



(b) Beam 1 – Thickness View.

Figure 48: Measurements for the first beam.

The measurements for the remaining three beams can be seen in Appendix A. The difference between the high and low values of the thickness side and the bending side are captured, and the difference is the warpage. The results are captured in Table 2.

	Beam 1	Beam 2	Beam 3	Beam 4
Warpage [mm]	1.3031	0.9603	1.3062	1.1497

Table 2: Tabulated results of warpage.

This yields an average warpage of 1.1798 mm.

Comparing that to the simulated results, where for 8 layers there is a warpage of 1.055 mm, the decrease in warpage for the simulations compared to the experiments is 10.58%. With the way the flash heating logic is applied in this work, as described in section 3.2, it makes sense that the simulations undershoot the true, experimental value, as the model only takes into account the mechanical response of previously sintered layers and not the layer currently being sintered.

4.1.4 Bridge Geometry

Having examined the beam geometry, the focus now shifts to a more complex geometry — the bridge — with the intent of measuring deformation using the bridge curvature method and possibly use DIC.

Both simulation and experimental investigations have been conducted for the bridge, as shown in Figs. 49 and 50.

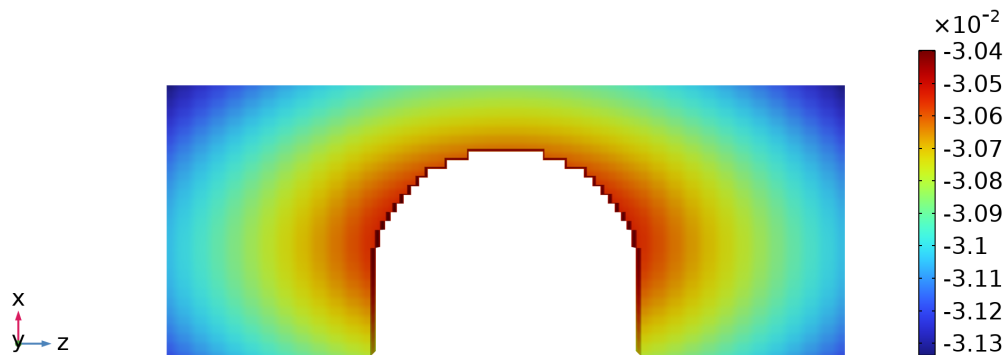


Figure 49: Strains in zz -direction and deformation at the end of the cooling phase, for 30 layer beam.



Figure 50: Picture of SLS printed bridge specimen.

No noticeable deformation can be observed in either of the two figures. While it is accurate that the simulation predicts no noticeable deformation, the inability to print a geometry that exhibits a more complicated warpage response than the beam is unfortunate, as it would have added to the validation of the simulation. This also means that the use of DIC isn't relevant in this project.

4.1.5 Parameter Study

With an idea of how the simulation behaves under normal processing conditions, now it can be investigated how changing different parameters affects the mechanical response of the beam. Specifically, the following section investigates the effect of doubling the beam thickness and increasing the laser power, two modifications that are expected to significantly affect warpage. By analyzing this, a greater understanding of the sensitivity of the simulation can be achieved. The final position in the build direction of a beam with thickness 6.4 mm is depicted in Fig. 51.

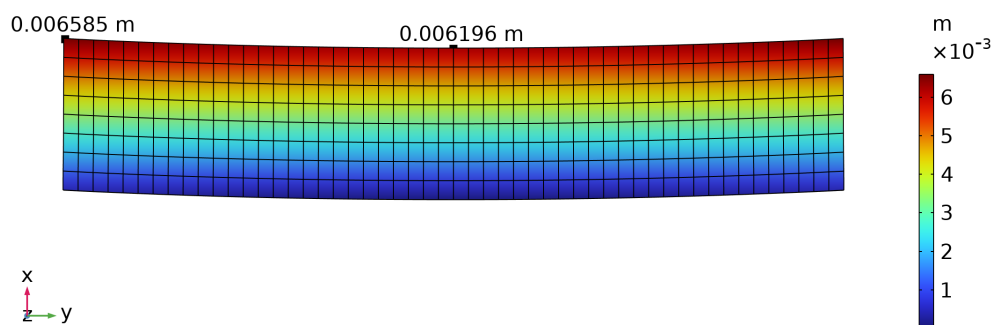


Figure 51: Position in the build direction after cooling phase for 8 layer beam with double thickness. Note that the x -axis has been stretched by a factor of 5 for visualization purposes.

The resulting warpage is 0.3886 mm, which is a large decrease from the beam with 3.2 mm thickness. Even though a thicker beam has a larger through-thickness temperature gradient

when cooling, less warpage is generally expected as the bending stiffness increases by the cube of the increase in thickness. To verify this two beams of thickness 6.4 mm was printed and experimentally measured for comparison. The added thickness meant the macroscope struggled to capture nice height plots near the edges of the beam. Thus a slightly different method of measurement is used, where the height is measured as the average along a line, see Figs. 57a - 57d in Appendix A. The warpage for the two thick beams was found to be 18.25 μm and 155.195 μm respectively. While the simulation correctly predicts a reduction in warpage, it fails to capture the fact that the warpage observed in the experiment is essentially negligible.

Next parameter to investigate is increasing the energy scale from 0.45 to 1 such that the laser power becomes the full 15.8 W. During this, the final position in the build direction is shown in Fig. 52.

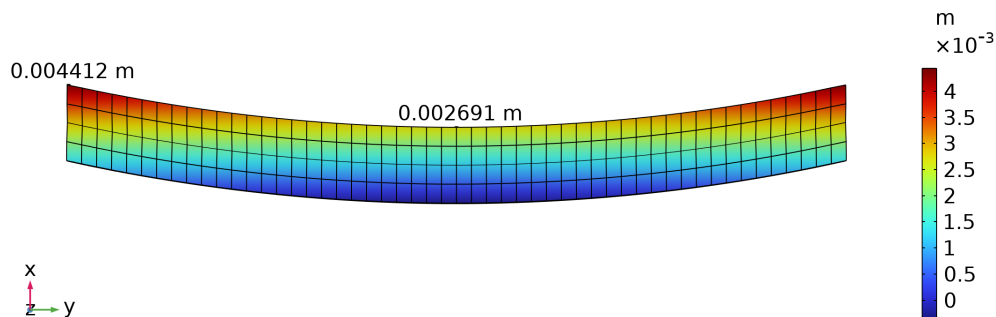


Figure 52: Position in the build direction after cooling phase for 8 layer beam with a laser power of 15.8 W. Note that the x-axis has been stretched by a factor of 5 for visualization purposes.

The warpage in this case is 1.7212 mm, which is a large increase from the beam with 7.11 W. Increasing laser power affects just the heating phase, where the temperature gradients become more severe, meaning the layers expand more, causing higher external, elastic and viscoplastic strains. While this makes sense theoretically, experimental investigation of this phenomenon was not conducted in the present work and is left for future study.

DISCUSSION

The simulations conducted throughout this project have, overall, demonstrated a good level of agreement with the experimental results. On a global scale, the deflection, shrinkage trends, and thermal gradients correspond fairly well to what was observed in the physical experiments and what is expected theoretically. However, it is important to note that this apparent agreement may involve, to a slight degree, incidental coincidence, rather than arising entirely from a perfectly fine-tuned model. The simulation is based on a series of assumptions and input parameters, and thus several key physical properties and boundary conditions within the simulation were not determined experimentally for our specific setup but were rather adopted from external sources. These include, but are not limited to, the heat transfer coefficients, viscoplastic parameters, and the dependency of density and shrinkage on cooling rate. Each of these parameters plays an important role in the accuracy of the simulation outputs, and their borrowed or estimated nature introduces an inherent fragility to the model's predictive capability. For instance, the heat transfer coefficient between the part and the powder bed was assumed constant, yet in reality, it is highly dependent on temperature, part geometry, and powder compaction, among other factors.

A more in-depth characterization of the material behavior could have significantly improved the model. Techniques such as differential scanning calorimetry (DSC) could have been used to investigate material parameters more thoroughly — specifically to assess the crystallization behavior, specific heat capacity, and thermal transitions critical for semi-crystalline polymers. Furthermore, the boundary condition used to simulate the powder bed could be improved, as there is some springiness to the surrounding powder that could have been modelled as a spring foundation.

In terms of geometry, the beam used for both the experiment and simulation is admittedly simple and arguably very well suited to the assumptions underlying the model. The absence of sharp curvatures or complex deformations means that the part response is not sufficiently challenging for the model to be properly validated in a more general sense. It would have been highly beneficial to test the model against a geometry with built-in curvature that warped — unlike the bridge geometry in Fig. 50. Such a scenario would potentially have allowed for the use of digital image correlation (DIC), which could offer a

more detailed strain distribution to validate the model against. This, in turn, would have helped expose any weaknesses or blind spots in the model.

Another area of improvement lies in the treatment of crystallization. The current model includes only a basic consideration of crystallization phases, yet it is well understood that the degree and kinetics of crystallization play a crucial role in polymer shrinkage and mechanical properties. Particularly, the presence of multiple crystallization phases and the timing of their onset have direct consequences for part warpage and final dimensions, as in this model, the shrinkage becomes "locked in" at a fixed transition temperature. Additionally, the shrinkage data the model uses (Fig. 7) is based on a constant cooling rate throughout the entire cooling phase. The model in this work only takes the shrinkage into account for the first part of the cooling phase — until the temperature decreases below the crystallization temperature. As the cooling rate is larger at the beginning, that means that my model predicts larger shrinkage than expected. Modelling recrystallization through an Avrami-type formulation (as in [9]) could provide a better prediction of the shrinkage during cooling.

Additionally, it is important to mention the clear differences between a flash heating model and a high-fidelity laser-scan-based model, as the flash heating model largely neglects the sintering dynamics that occur just around the melting point. These processes — where the polymer transitions from powder to melt and then re-solidifies — are inherently complex and involve not just thermal but also rheological and surface tension-driven behaviors. In the current framework, these effects are either oversimplified or not captured at all, which limits the model's ability to predict early-stage densification and associated shrinkage patterns.

With regard to the viscoplastic model used, it too could have been explored in greater depth. While a basic viscoplastic approach was adopted, more sophisticated models exist, such as those proposed by Bergström that are based on the Arruda–Boyce framework or Flow Evolution Networks [28]. These offer a richer and more physically grounded description of viscoplastic flow in polymers. Complementary to this, a dynamic mechanical analysis (DMA) could have been performed to empirically determine time-dependent modulus variations and viscoelastic responses across the relevant temperature range.

Experiment-wise, it is worth noting that three of the beams used for validation were printed in a shared build chamber with other parts present. The number of parts was kept low (3-4 parts), and they were placed at a distance to minimize thermal interaction, but their presence still introduces a variable that is not reflected in the simulation. Ideally,

the model would be capable of including such environmental effects, possibly through a chamber-scale thermal simulation that includes multiple parts.

Additionally, considering the measurement of the deflection of the beams, there can be inaccuracies if the beam exhibits subtle transverse bending. An unnoticeable lift at the measurement points could skew results, especially since the deformations being measured are on such a small scale.

Furthermore, from a numerical standpoint, there is room for improvement. The current model operated on a reduced number of layers due to computational constraints. A model with the true layer height of 0.1 – 0.125 mm would more faithfully represent the actual build and would likely produce results with greater resolution and fidelity, particularly in the vertical dimension. However, the required computational resources were not available during this study.

An interesting thing to explore would have been to reverse the activation logic within the model. Currently, the model is somewhat conservative and tends to underpredict deformation. By activating during heating and thus overestimating warpage, it could be possible to generate a worst-case scenario simulation. In many engineering contexts, particularly those concerning safety, such overshooting could actually be more valuable than underprediction. This version of the model could serve as an upper-bound estimator for process-induced distortions.

Regarding the broader utility of this work, the simulation presented here represents an interesting starting point. Although it is not yet optimized for speed, the framework might have the potential to offer a faster alternative to more complex laser-scan-based simulations. While it lacks the resolution to capture localized thermal or mechanical phenomena, it may be particularly well-suited for large-batch printing scenarios — such as batch fabrication of tensile test specimens or other slender structures. In these cases, understanding the general deformation trend and cooling-induced shrinkage can be used for part-orientation strategies and chamber layout planning. The ability to predict whether such objects can be printed successfully in a specific orientation or under altered cooling conditions (e.g., with increased convection to save on cooling time), or if the warpage has an effect on fit tolerance, could lead to time and resource savings in industrial settings.

CONCLUSION

In this study, a model has been created that can be used to predict the warpage of a part. The model is based on a flash heating approach, where an entire layer is heated at once. Within the framework of this approach, the thermal behavior is accurately modelled, which is essential for capturing the temperature-dependent properties that govern material response during printing and cooling. Specifically, the material responses most critical to modelling warpage in this work are the development of strains caused by density changes and the viscoplastic deformation that occurs near the melting point.

The simulations presented in this study demonstrate that it is possible to create a model for SLS printing that aligns reasonably well with experimental results for warpage. On average a 10.58% underestimation in total warpage was observed in the simulations compared to experimental measurements. However, the overall trends in deflection, material response, and thermal behavior were captured with notable consistency and aligned well with both theoretical expectations and experimental observations. The agreement with theoretical expectations is illustrated by the parameter study, where the simulation correctly predicts reduced warpage for thicker beams. However, it does not capture the near absence of warpage observed experimentally in these cases. For the laser power study, although no experimental data is available for direct comparison, the simulation predicts increased warpage with higher laser power, which aligns with theoretical understanding.

A critical reflection on the current model reveals that much of the model's predictive success is likely due to fortuitous parameter selection rather than perfect calibration to the specific experimental system. The model is based on assumptions and literature-derived parameters rather than experimentally verified input from our own material and printer.

Despite these limitations, the simulation provides a promising foundation. Its strength lies in its potential efficiency, where it could offer a faster alternative to laser-scanning-based simulations for broader process planning or batch evaluation. For large-scale production involving simple geometries — like tensile bars or long, slender parts — this type of model could be a valuable tool for assessing printability, evaluating orientation strategies, and estimating print time savings via increased cooling rates.

FUTURE WORK

Looking ahead, there are several ways to make the model more robust and realistic. First, a range of experiments could be conducted to determine the thermal and mechanical parameters thoroughly — using methods like DSC and DMA — this would reduce the reliance on external data. Secondly, incorporating the recrystallization behavior more directly through, e.g., an Avrami model would help to achieve more true-to-life shrinkage and improve the prediction of final part geometry.

Future work should also explore the behavior of the model for more complex scenarios. Curved geometries, bridge-like structures, or forced cooling scenarios could better challenge the assumptions of the model and validate its performance. Finally, increasing the number of simulated layers along with optimizing the computational efficiency could allow the model to deliver higher-resolution predictions at, hopefully, a fast pace.

By pursuing these directions, the model developed in this work might evolve from an early prototype into a valuable process simulation tool that is capable not only of fast predictions but also of providing reliable insights into shrinkage and deformation for SLS printing.

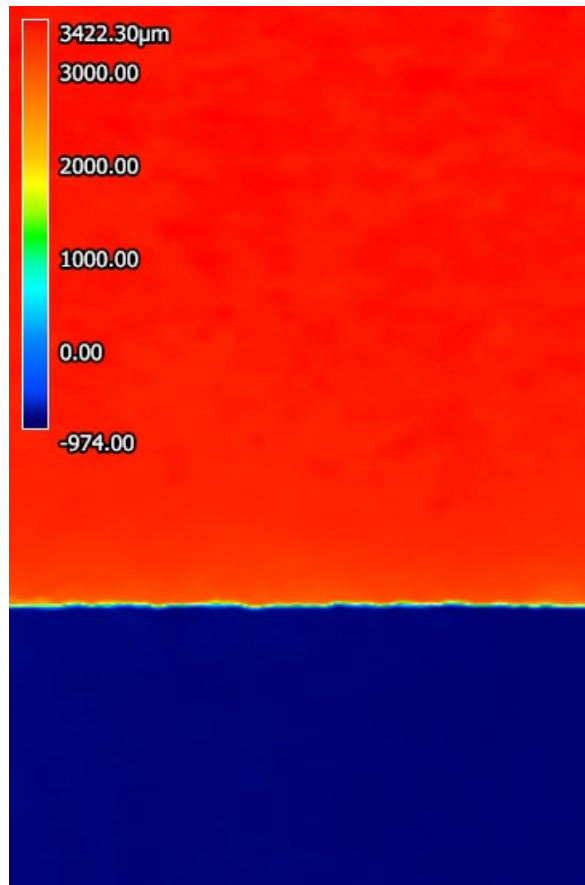
BIBLIOGRAPHY

- [1] A. Thorsen. Development of a thermal model for SLS printing using a flash heating approach (2024). Master's thesis preproject, Aarhus University
- [2] COMSOL. Understanding and changing the element order. [Link](#), [Accessed: 08-05-2025]
- [3] C. Saraf. The ultimate guide for selective laser sintering (SLS): Process, materials, applications, advantages, disadvantages (2024). [Link](#), [Accessed: 13-03-2025]
- [4] Sinterit. Sinterit Lisa X original user manual (2022). [Link](#), [Accessed: 22-04-2025]
- [5] Sinterit. Sinterit Lisa X product specification (2022). [Link](#), [Accessed: 22-04-2025]
- [6] M. Bayat, C.G. Klingaa, S. Mohanty, D. De Baere, J. Thorborg, N.S. Tiedje, J.H. Hattel, Part-scale thermo-mechanical modelling of distortions in laser powder bed fusion – analysis of the sequential flash heating method with experimental validation, *Additive Manufacturing* **36** (2020). DOI <https://doi.org/10.1016/j.addma.2020.101508>
- [7] D. Riedlbauer, M. Drexler, D. Drummer, P. Steinmann, J. Mergheim, Modelling, simulation and experimental validation of heat transfer in selective laser melting of the polymeric material PA12, *Computational Materials Science* **93** (2014). DOI <https://doi.org/10.1016/j.commatsci.2014.06.046>
- [8] Z.D. Zhang, S. Imani Shahabad, O. Ibhadode, C.F. Dibia, A. Bonakdar, E. Toyserkani, 3-dimensional heat transfer modeling for laser powder bed fusion additive manufacturing using parallel computing and adaptive mesh, *Optics & Laser Technology* **158** (2023). DOI <https://doi.org/10.1016/j.optlastec.2022.108839>
- [9] F. Shen, W. Zhu, K. Zhou, et al., Modeling the temperature, crystallization, and residual stress for selective laser sintering of polymeric powder, *Acta Mechanica* **232** (2021). DOI <https://doi.org/10.1007/s00707-021-03020-6>

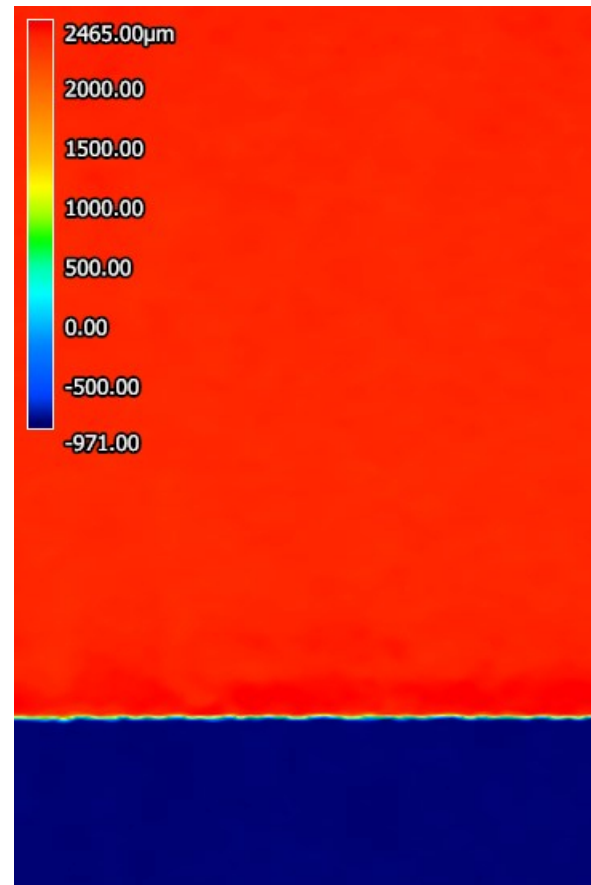
- [10] J. Li, S. Yuan, J. Zhu, S. Li, W. Zhang, Numerical model and experimental validation for laser sinterable semi-crystalline polymer: Shrinkage and warping, *Polymers* **12** (2020). DOI <https://doi.org/10.3390/polym12061373>
- [11] H.W.B. Teo, K. Chen, V.T. Tran, H. Du, J. Zeng, K. Zhou, Non-isothermal crystallization behaviour of polyamide 12 analogous to multi-jet fusion additive manufacturing process, *Polymer* **235** (2021). DOI <https://doi.org/10.1016/j.polymer.2021.124256>
- [12] M. Issametova, N.V. Martyushev, A. Zhastalap, L.B. Sabirova, U. Assemgul, A. Tursynbayeva, G. Abilezova, Determination of residual stresses in 3D-printed polymer parts, *Polymers* **16**(14) (2024). DOI <https://doi.org/10.3390/polym16142067>
- [13] I. Gibson, D. Rosen, B. Stucker, M. Khorasani, *Additive Manufacturing Technologies*, 3rd edn. (Springer, 2014)
- [14] Y.A. Cengel, A.J. Ghajar, *Heat and Mass Transfer - Fundamental & Applications*, 5th edn. (McGraw Hill, 2014)
- [15] C. Li, S.E. Snarr, E.R. Denlinger, J.E. Irwin, M.F. Gouge, P. Michaleris, J.J. Beaman, Experimental parameter identification for part-scale thermal modeling of selective laser sintering of PA12, *Additive Manufacturing* **48** (2021). DOI <https://doi.org/10.1016/j.addma.2021.102362>
- [16] J. Hesselvig, R.T. Nygaard. Studying SLS-printing through multiphysics thermal and flow analysis with experimental validation (2024). Bachelor's Project, Aarhus University
- [17] P. Peyre, Y. Rouchausse, D. Defauchy, G. Régnier, Experimental and numerical analysis of the selective laser sintering (SLS) of PA12 and PEKK semi-crystalline polymers, *Journal of Materials Processing Technology* **225** (2015). DOI <https://doi.org/10.1016/j.jmatprotec.2015.04.030>
- [18] COMSOL. Thermal modeling of phase change materials with hysteresis (2016). [Link](#), [Accessed: 10-03-2025]
- [19] Y.A. Cengel, M.A. Boles, A.J. Ghajar, M. Kanoğlu, *Thermodynamics An Engineering Approach*, 9th edn. (McGraw Hill, 2019)
- [20] F. Thümmler, R. Oberacker, *Introduction to Powder Metallurgy* (The Institute of Materials, 1993)

- [21] L. Dong, A. Makradi, S. Ahzi, Y. Remond, Three-dimensional transient finite element analysis of the selective laser sintering process, *Journal of Materials Processing Technology* **209**(2) (2009). DOI <https://doi.org/10.1016/j.jmatprotec.2008.02.040>
- [22] P.L. Gould, Y. Feng, *Introduction to Linear Elasticity*, 4th edn. (Springer International Publishing, 2018)
- [23] K. Hashiguchi, *Elastoplasticity Theory*, 2nd edn. (Springer, 2014)
- [24] J.H. Ferziger, M. Peric, R.L. Street, *Computational Methods for Fluid Dynamics*, 4th edn. (Springer, 2020)
- [25] ABAQUS Inc. Spurious oscillations due to small time increments (2006). ABAQUS User's Manual, Version 6.6, Section 6.5.2
- [26] K. Corporation. VR-3200 wide-area 3D measurement system macroscope head. [Link](#), [Accessed: 19-05-2025]
- [27] J.P. Kruth, J. Deckers, E. Yasa, R. Wauthle, Assessing influencing factors of residual stresses in slm using a novel analysis method, *16th International Symposium on Electromachining, ISEM 2010* pp. 531–537 (2010)
- [28] D.W. Abueidda, M. Bakir, R.K.A. Al-Rub, J.S. Bergström, N.A. Sobh, I. Jasiuk, Mechanical properties of 3D printed polymeric cellular materials with triply periodic minimal surface architectures, *Materials & Design* **122** (2017). DOI <https://doi.org/10.1016/j.matdes.2017.03.018>

APPENDIX: EXPERIMENTAL MEASUREMENTS

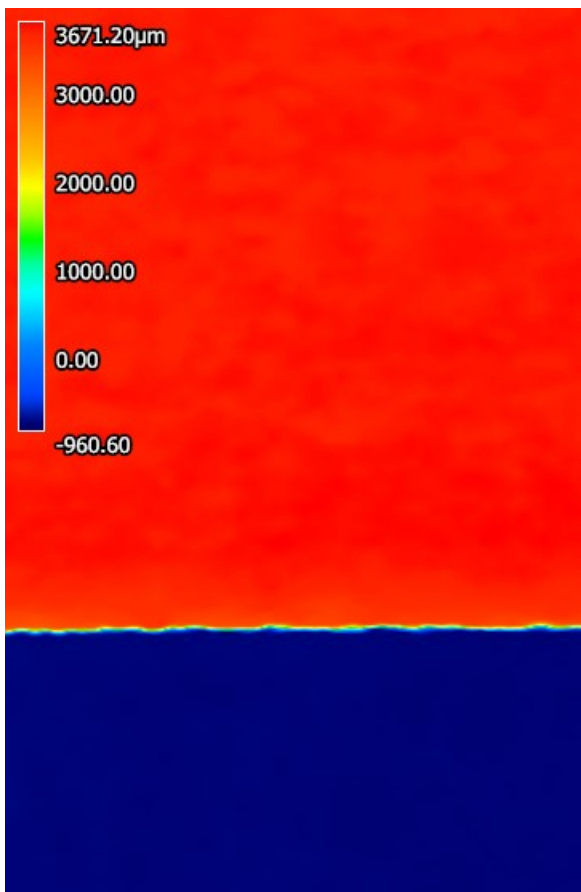


(a) Beam 2 – bend view.

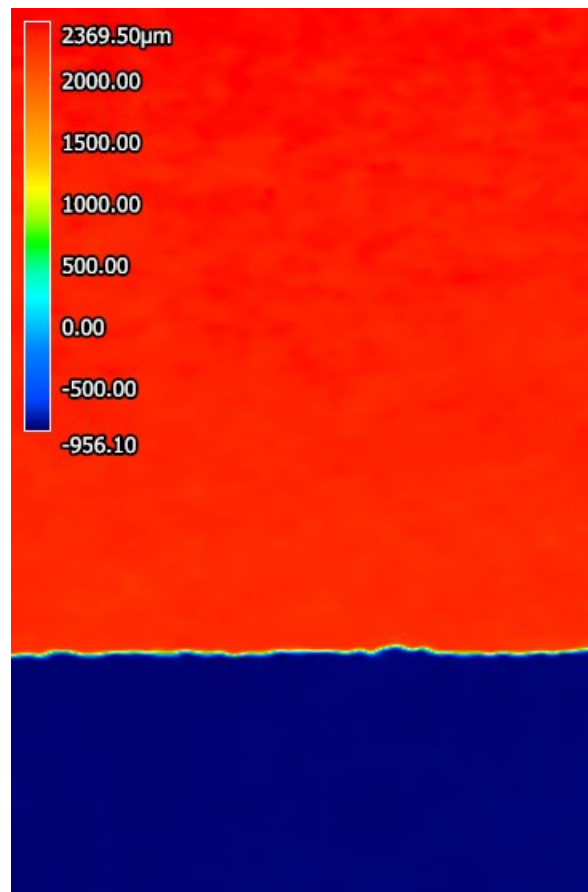


(b) Beam 2 – thickness view.

Figure 53: Measurements for the second beam

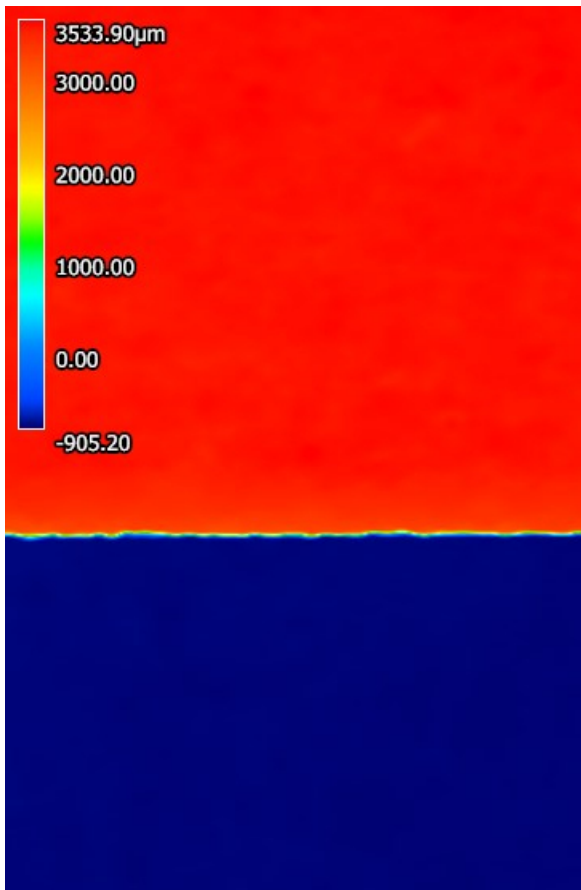


(a) Beam 3 – bend view.

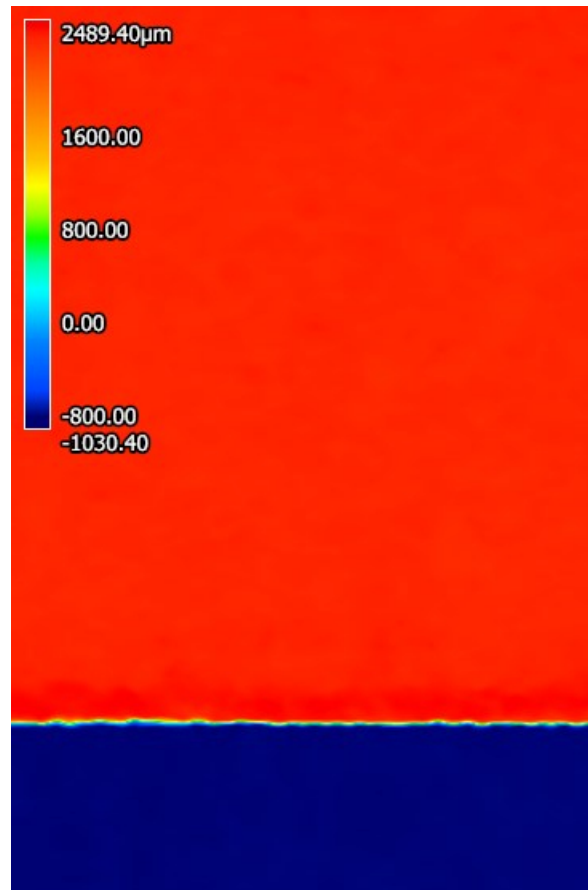


(b) Beam 3 – thickness view.

Figure 54: Measurements for the third beam



(a) Beam 4 – bend view.



(b) Beam 4 – thickness view.

Figure 55: Measurements for the fourth beam

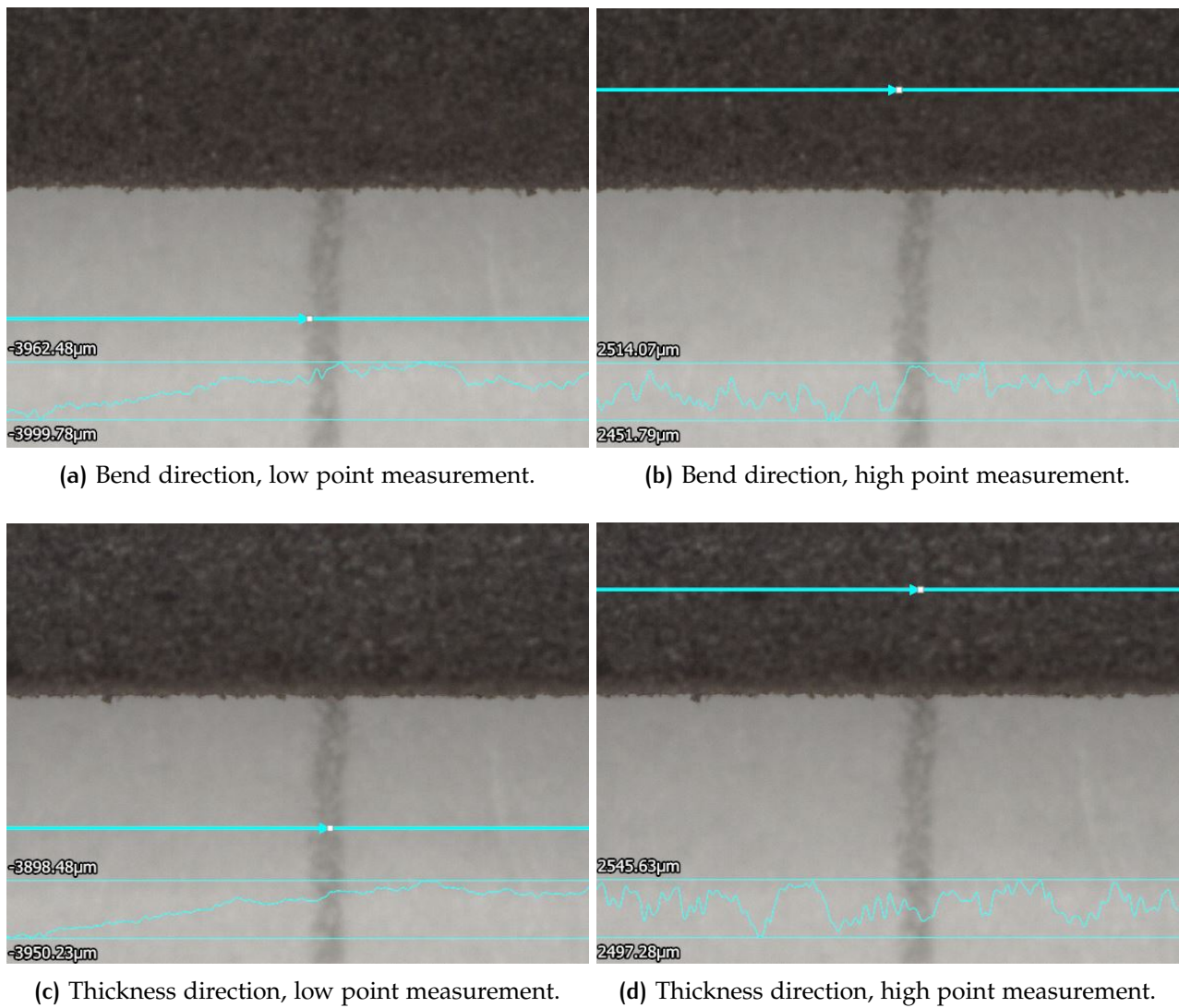


Figure 56: Thick beam 1 measurements.

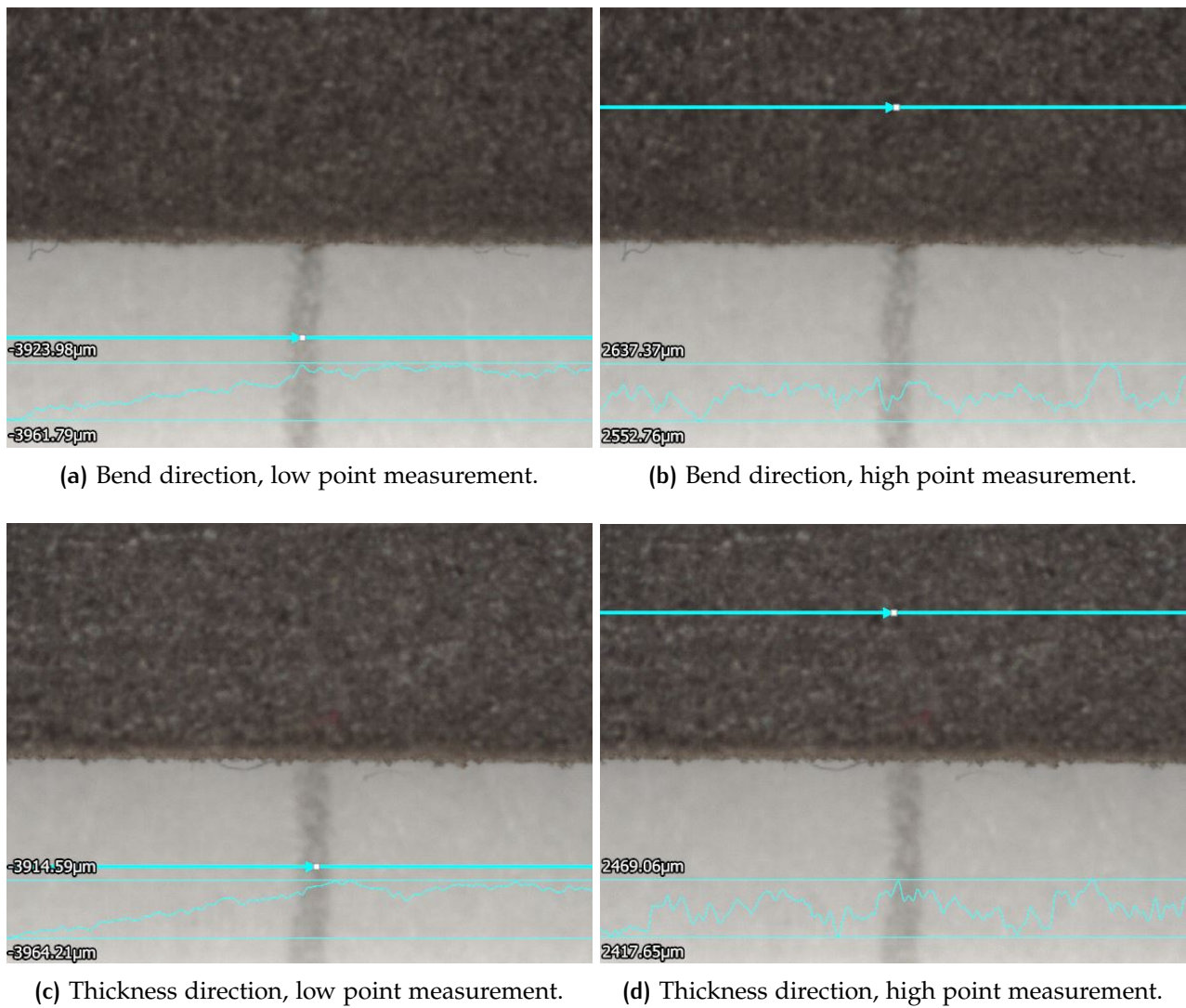


Figure 57: Thick beam 2 measurements.

Declaration of use of GAI tools

I/we used generative artificial intelligence (GAI) to complete this project
(tick the box). List the GAI tool(s) you used (remember to specify version):

- ChatGPT 3.5
- ChatGPT 4

I/we used GAI tools in the following way (*See accompanying list of possible uses for inspiration*)

- For feedback on own text
- For alternative ways of formulating text
- For punctuation and grammar
- To understand a topic better
- For programming tasks, such as creating the code that plots figures in MATLAB.